MR3522: Tropical Meteorology

Hadley Cell and Walker Circulation

Main Topics:

- Hadley cell
- Intertropical Convergence Zone (ITCZ)
- Shallow circulation in ITCZ
- Inertial instability and cross-equatorial flow

Module 4.1

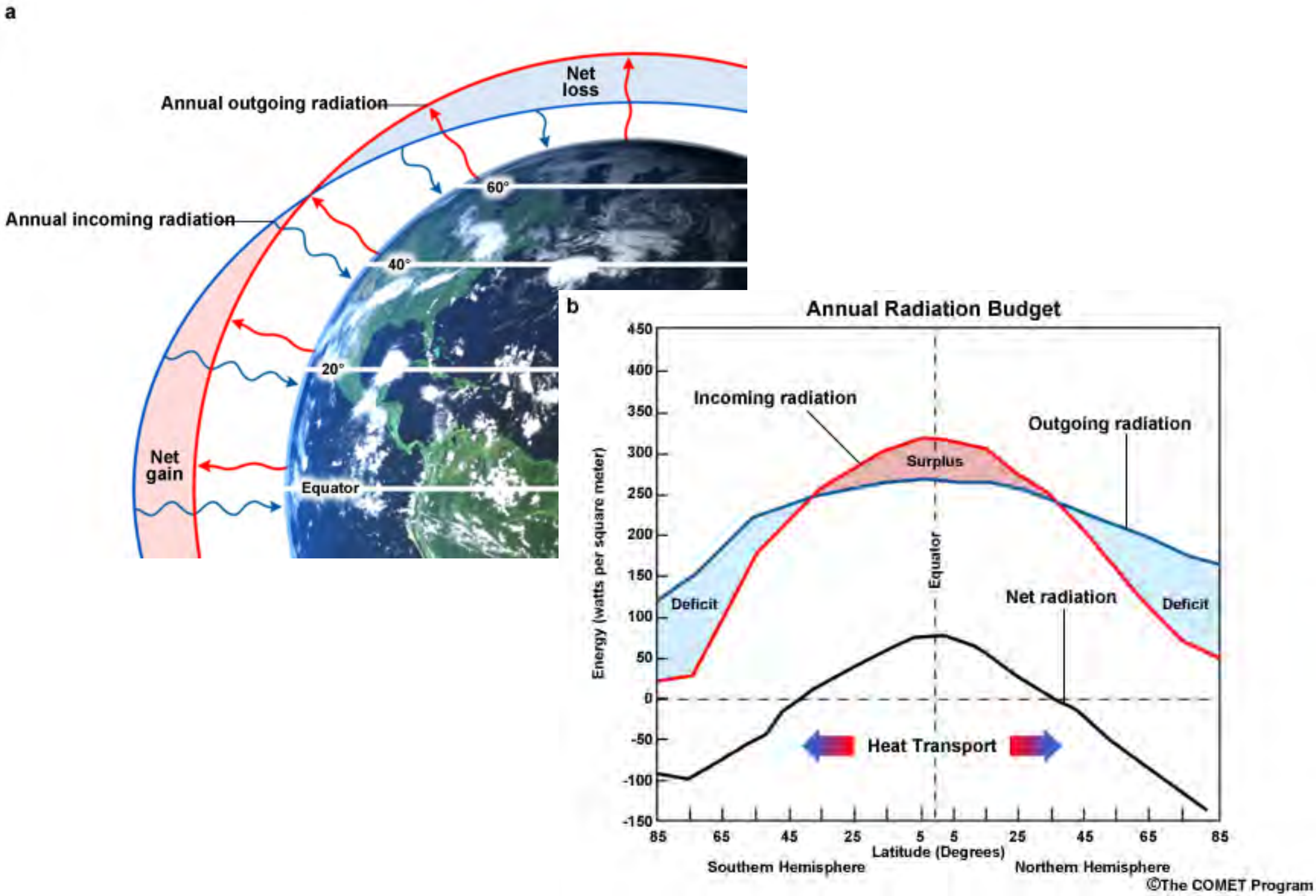

a
Annual outgoing radiation
Net loss
Annual incoming radiation
60°
40°
20°
Equator
Net gain
b
Annual Radiation Budget
Incoming radiation
Outgoing radiation
Surplus
Deficit
Deficit
Equator
Net radiation
Heat Transport
Energy (watts per square meter)
450
400
350
300
250
200
150
100
50
0
-50
-100
-150
85 65 45 25 5 5 25 45 65 85
Latitude (Degrees)
Southern Hemisphere
Northern Hemisphere
©The COMET Program

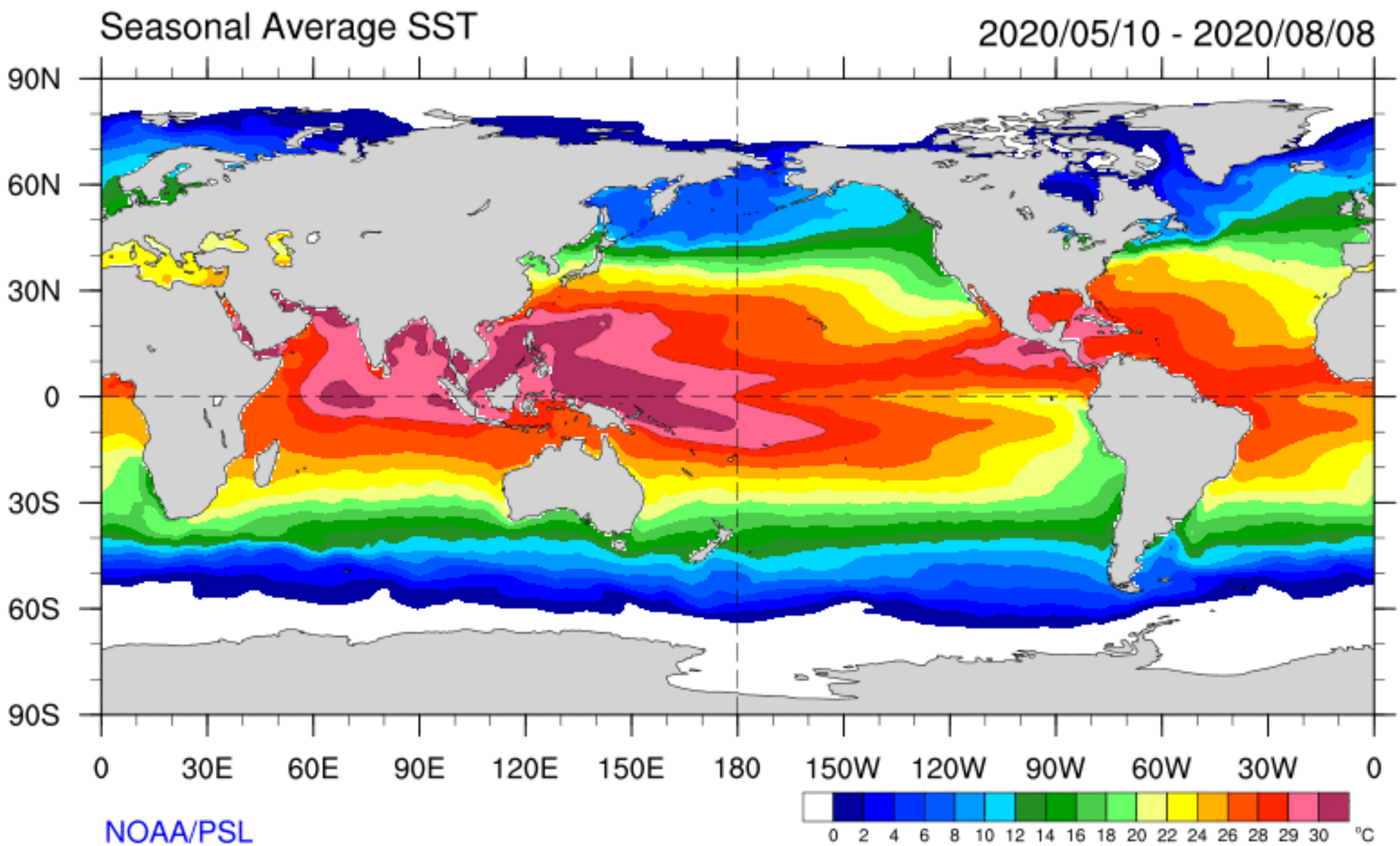

Seasonal Average SST
2020/05/10 - 2020/08/08
90N
60N
30N
0
30S
60S
90S
0
30E
60E
90E
120E
150E
180
150W
120W
90W
60W
30W
0
NOAA/PSL
0 2 4 6 8 10 12 14 16 18 20 22 24 26 28 29 30
°C

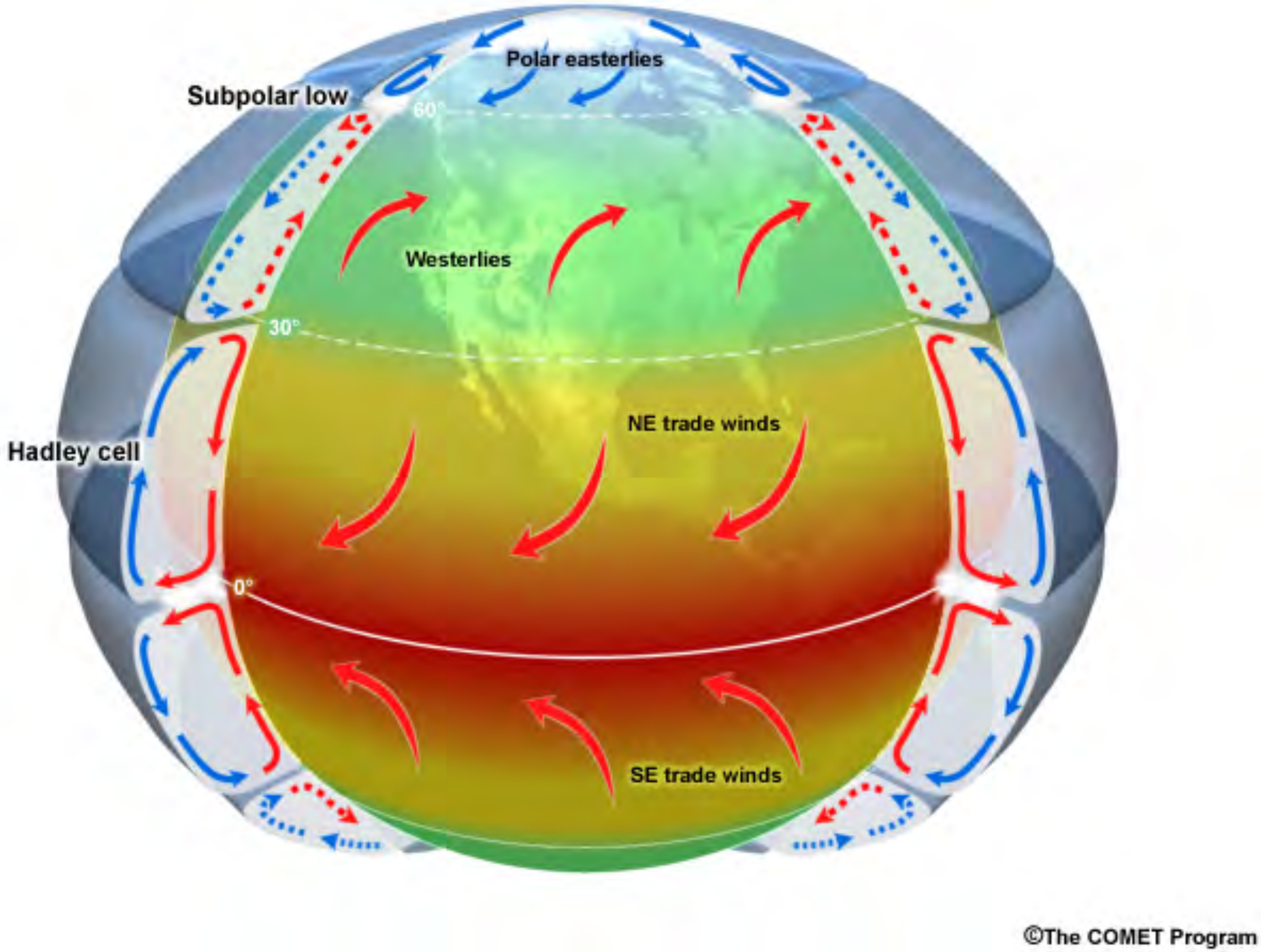

Hadley cell (Halley 1686; Hadley 1735)

Waliser and Gautier (1993)

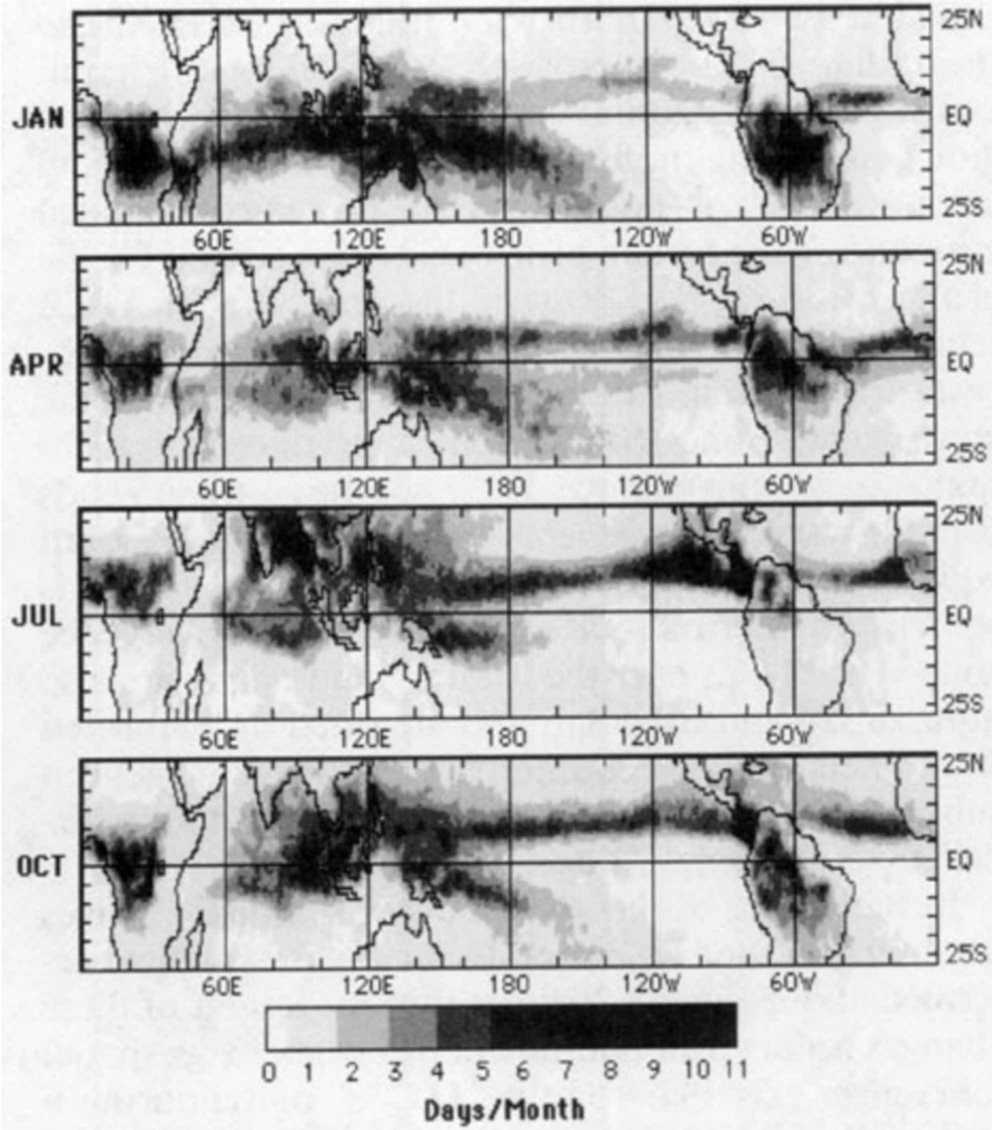

FIG. 1. Mean monthly "ITCZ" structure for the months: (a) January, (b) April, (c) July, and (d) October. These mean monthly images were computed from 17 years of monthly HRC data. Values represent the number of days per month (sampled once per day) the given grid point was covered by a large-scale deep convective system (subjectively determined; see section 2).

Hack et al. (1989)

Heating at 10°N

Heating at equator

Normalized meridional streamflow

Zonal Wind

Temperature perturbation

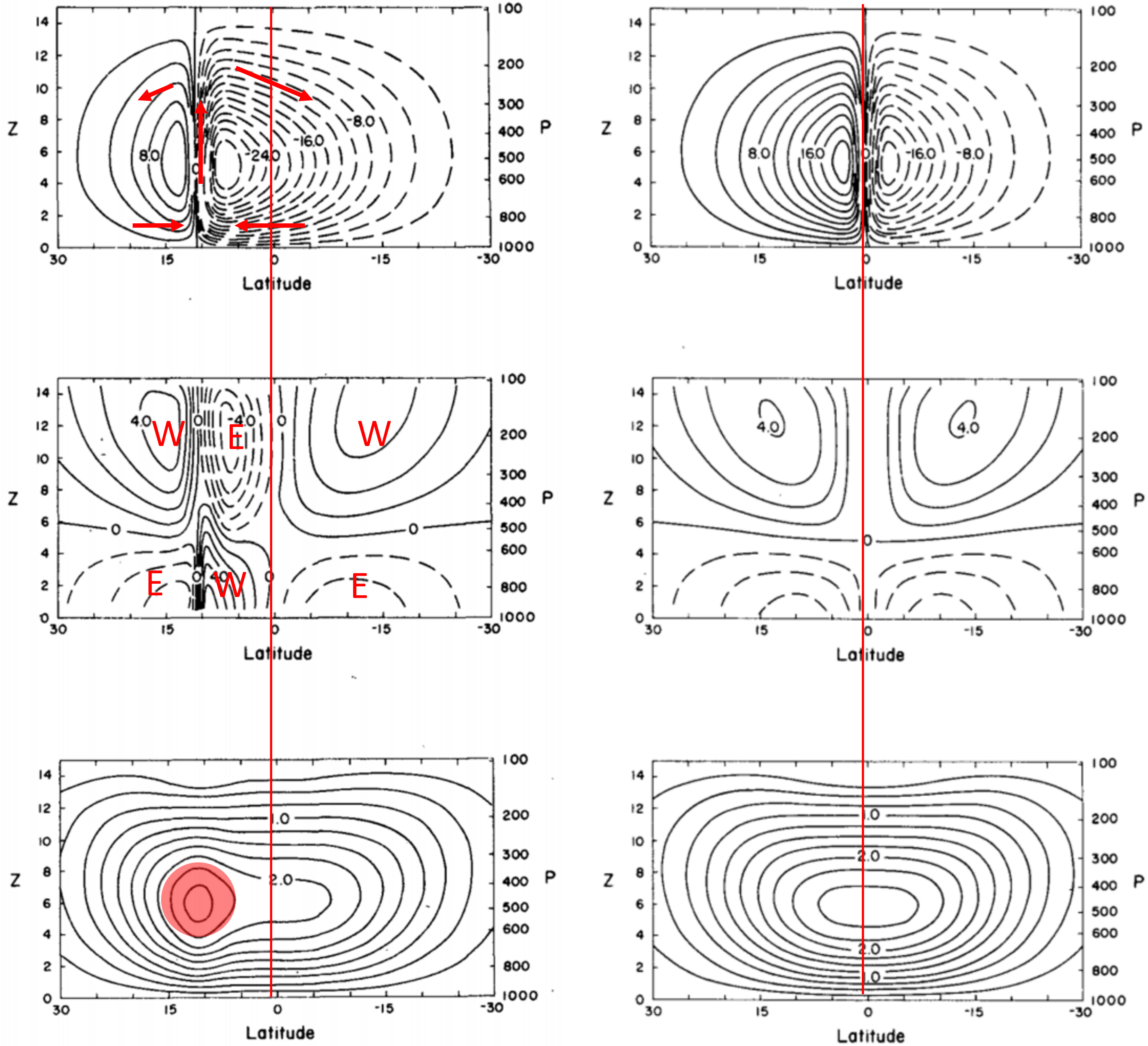

A shallow return flow in the ITCZ where meridional gradients of SST are large

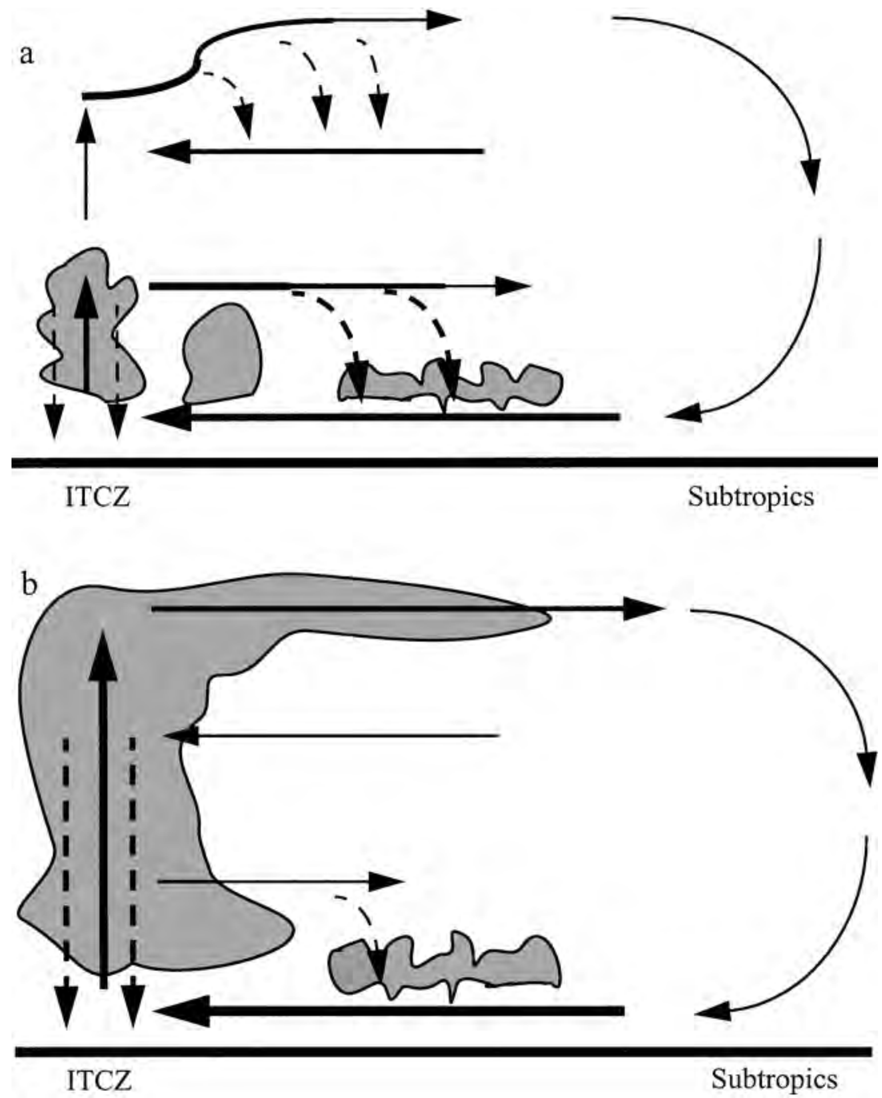

Nolan et al. (2007)

Simulated budgets of mass, water, and MSE into/out of ITCZ in EPAC

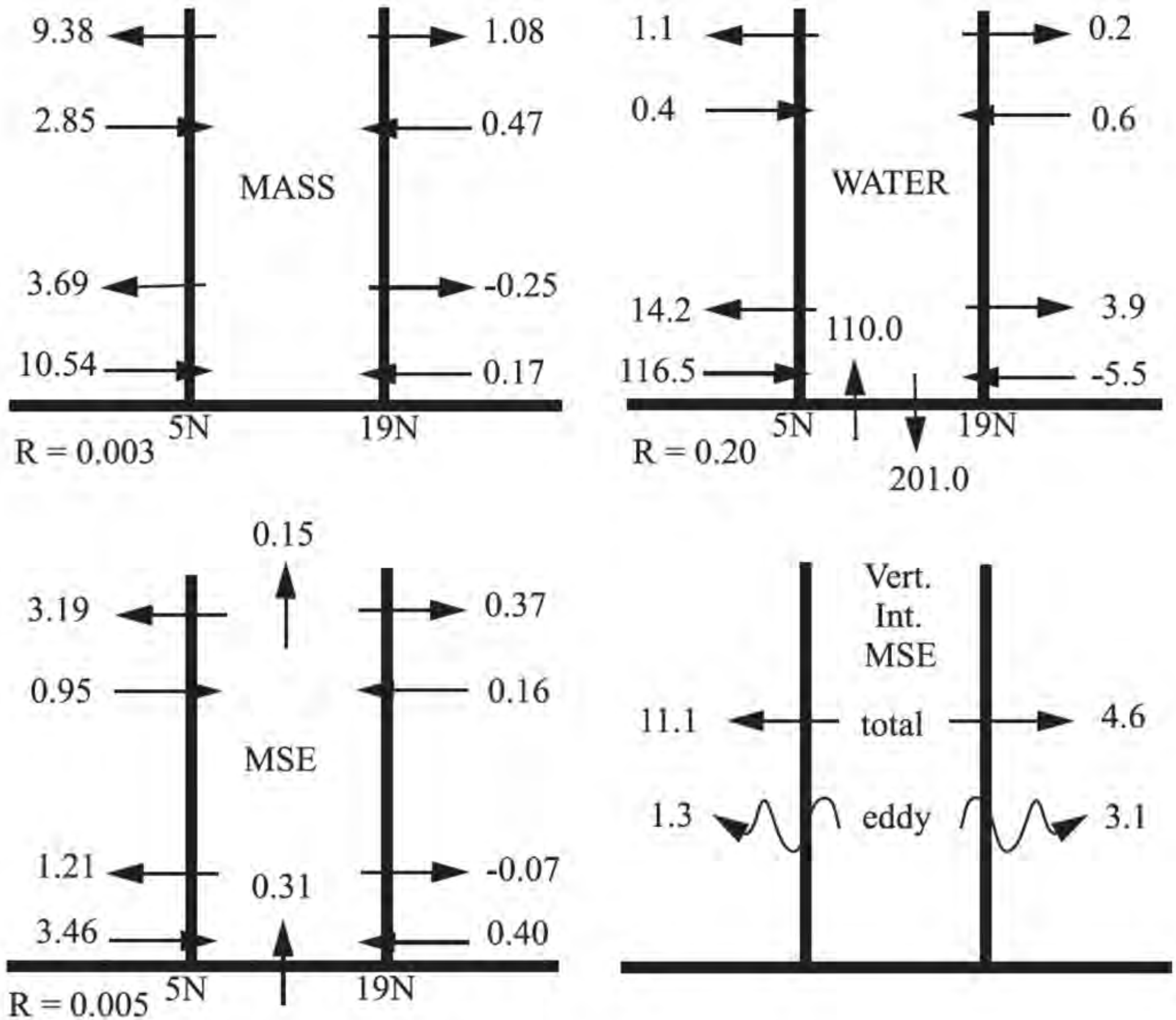

Nolan et al. (2010)

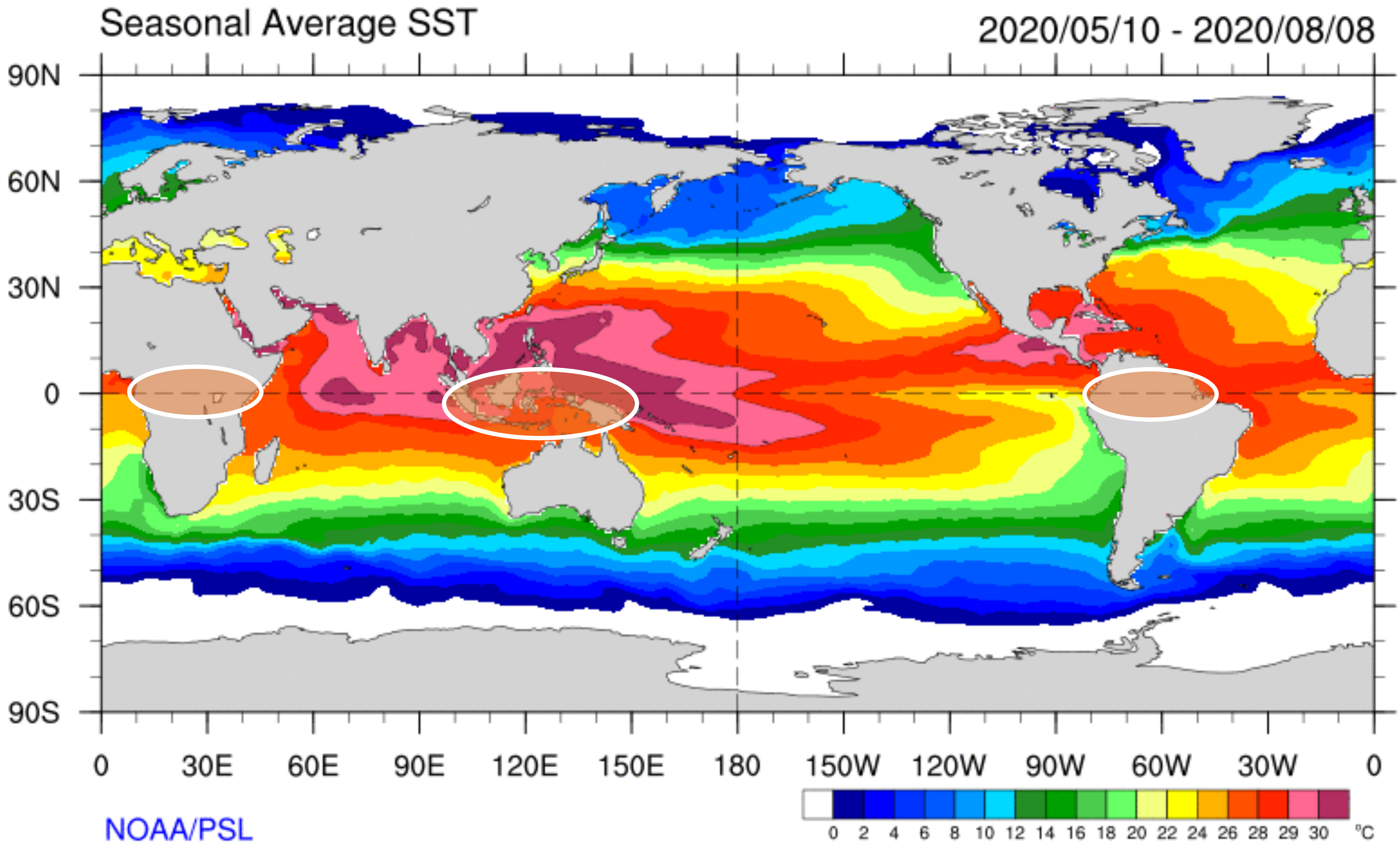

Seasonal Average SST
2020/05/10 - 2020/08/08
90N
60N
30N
0
30S
60S
90S
0
30E
60E
90E
120E
150E
180
150W
120W
90W
60W
30W
0
NOAA/PSL
0 2 4 6 8 10 12 14 16 18 20 22 24 26 28 29 30
°C

Gill (1980)

$$\varepsilon u - \frac{vy}{2} = -\frac{\partial p}{\partial x}$$

$$\varepsilon v - \frac{uy}{2} = -\frac{\partial p}{\partial y}$$

$$\varepsilon p + \frac{\partial u}{\partial x} + \frac{\partial v}{\partial y} = -Q$$

$$w = \varepsilon p + Q$$

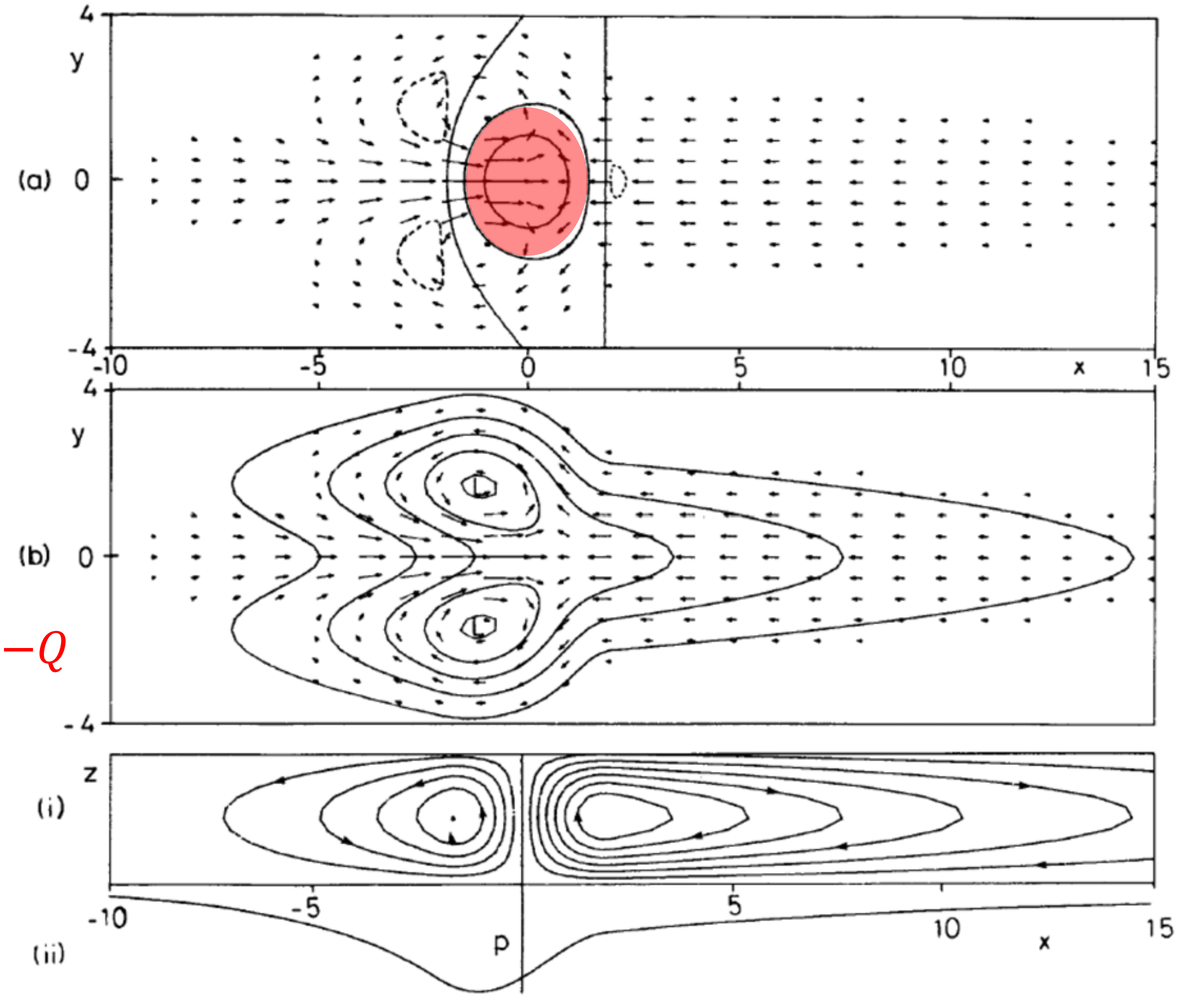

Figure 1. Solution for heating symmetric about the equator in the region $|x| < 2$ for decay factor $\varepsilon = 0{\cdot}1$.
(a) Contours of vertical velocity w (solid contours are 0, 0·3, 0·6, broken contour is −0·1) superimposed on the velocity field for the lower layer. The field is dominated by the upward motion in the heating region where it has approximately the same shape as the heating function. Elsewhere there is subsidence with the same pattern as the pressure field.

(b) Contours of perturbation pressure p (contour interval 0·3) which is everywhere negative. There is a trough at the equator in the easterly régime to the east of the forcing region. On the other hand, the pressure in the westerlies to the west of the forcing region, though depressed, is high relative to its value off the equator. Two cyclones are found on the north-west and south-west flanks of the forcing region.

(c) The meridionally integrated flow showing (i) stream function contours, and (ii) perturbation pressure. Note the rising motion in the heating region (where there is a trough) and subsidence elsewhere. The circulation in the right-hand (Walker) cell is five times that in each of the Hadley cells shown in (c).

ε is a frictional dissipation or Newtonian cooling term that replaces $\frac{\partial}{\partial t}$.

Gill (1980)

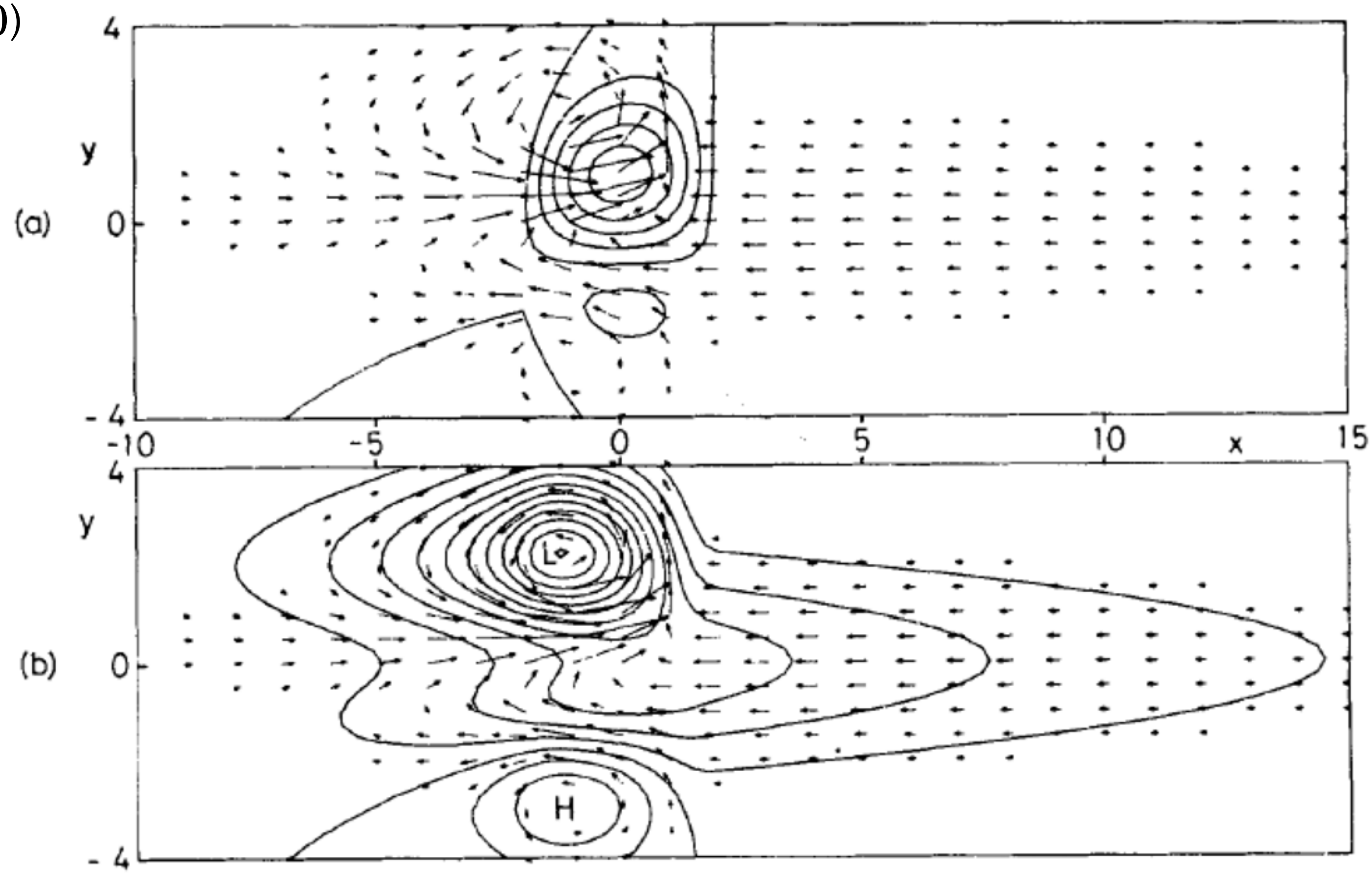

Figure 3. Solution obtained by adding the solutions shown in the two previous figures, corresponding to heating which is confined to the region $|x| < 2$ and is mainly concentrated to the north of the equator. (a) Contours of vertical velocity w (contour interval 0·3) showing the dominance of the heating north of the equator. The flow to the east of the forcing region is the same as in Fig. 1, this being provided entirely by the symmetric part of the heating. West of the forcing, the westerly inflow is concentrated between the equator and $y = 2$. An easterly flow is found south of the equator.

(b) Contours of perturbation pressure p (contour interval 0·3). The pattern is dominated by a low on the western flank of the heating region and by the equatorial trough. A high is found in the southern hemisphere.

Gill (1980)

Symmetric heating

Asymmetric heating in North

u

ψ

p′

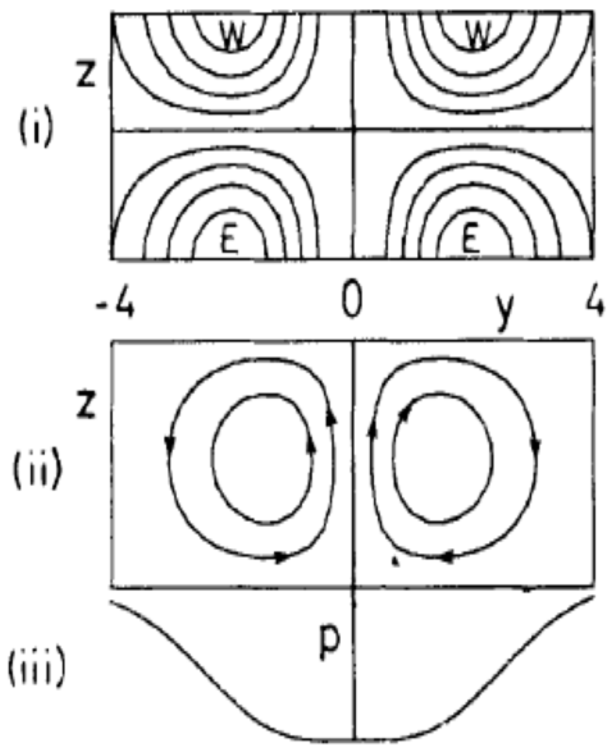

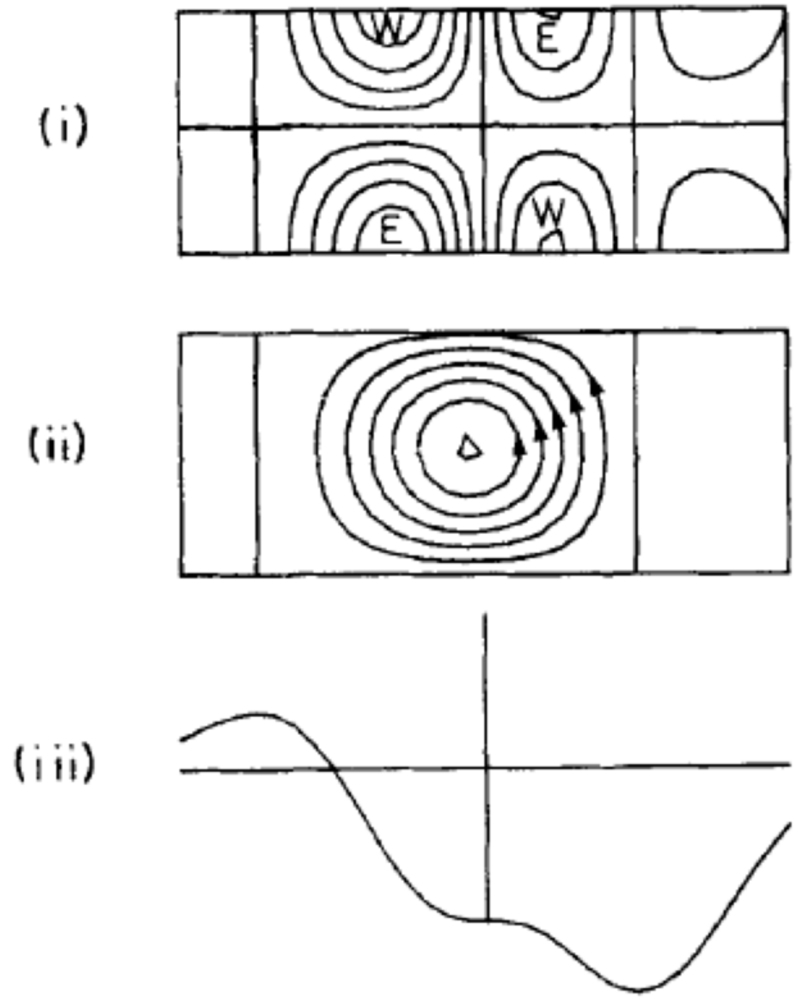

NOAA

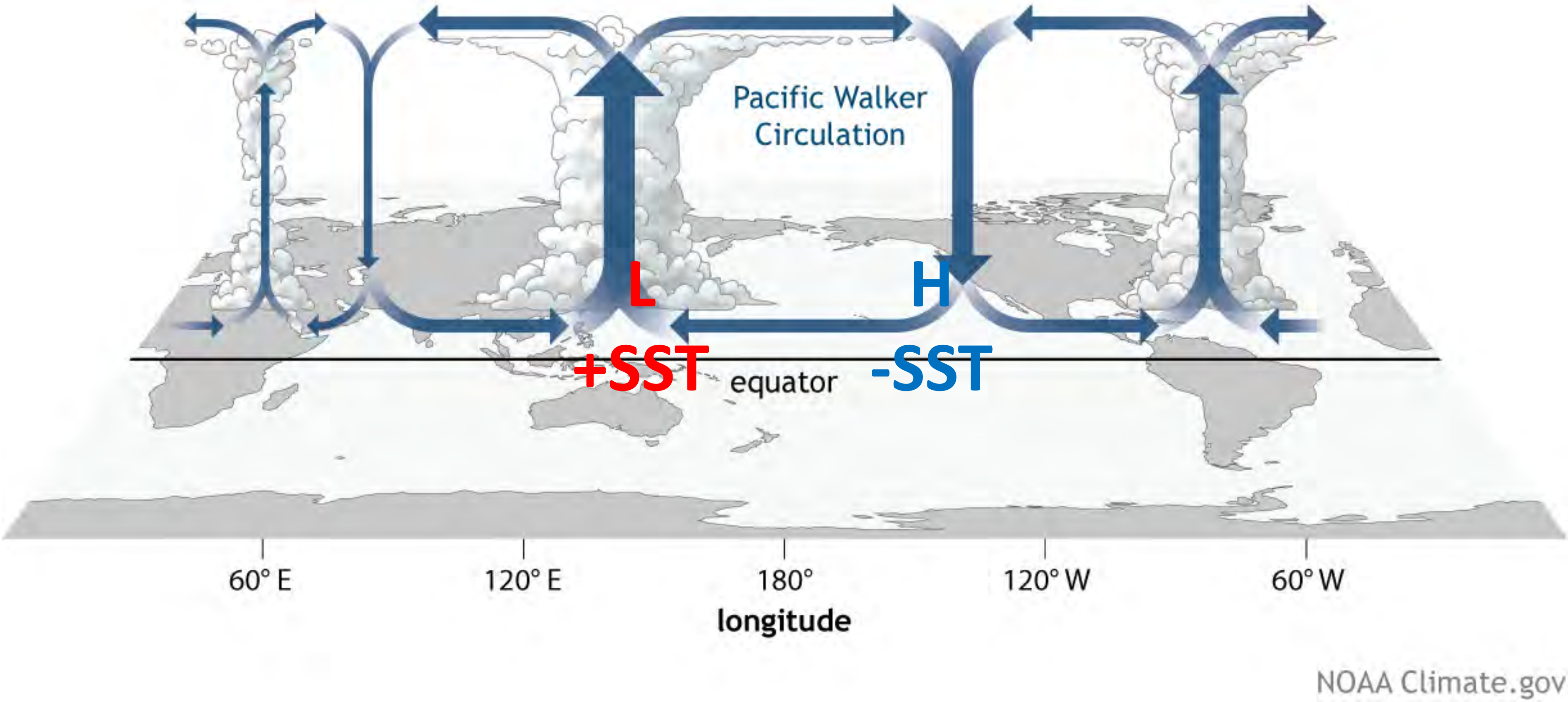

Pacific Walker Circulation
L
H
+SST
-SST
equator
60° E
120° E
180°
120° W
60° W
longitude
NOAA Climate.gov

MR3522: Tropical Meteorology

Coupled Atmosphere-Ocean Variability in the Walker Cells

Main Topics:

- Qualitative descriptions of
  - El Niño-Southern Oscillation
  - Indian Ocean Dipole

Module 4.2

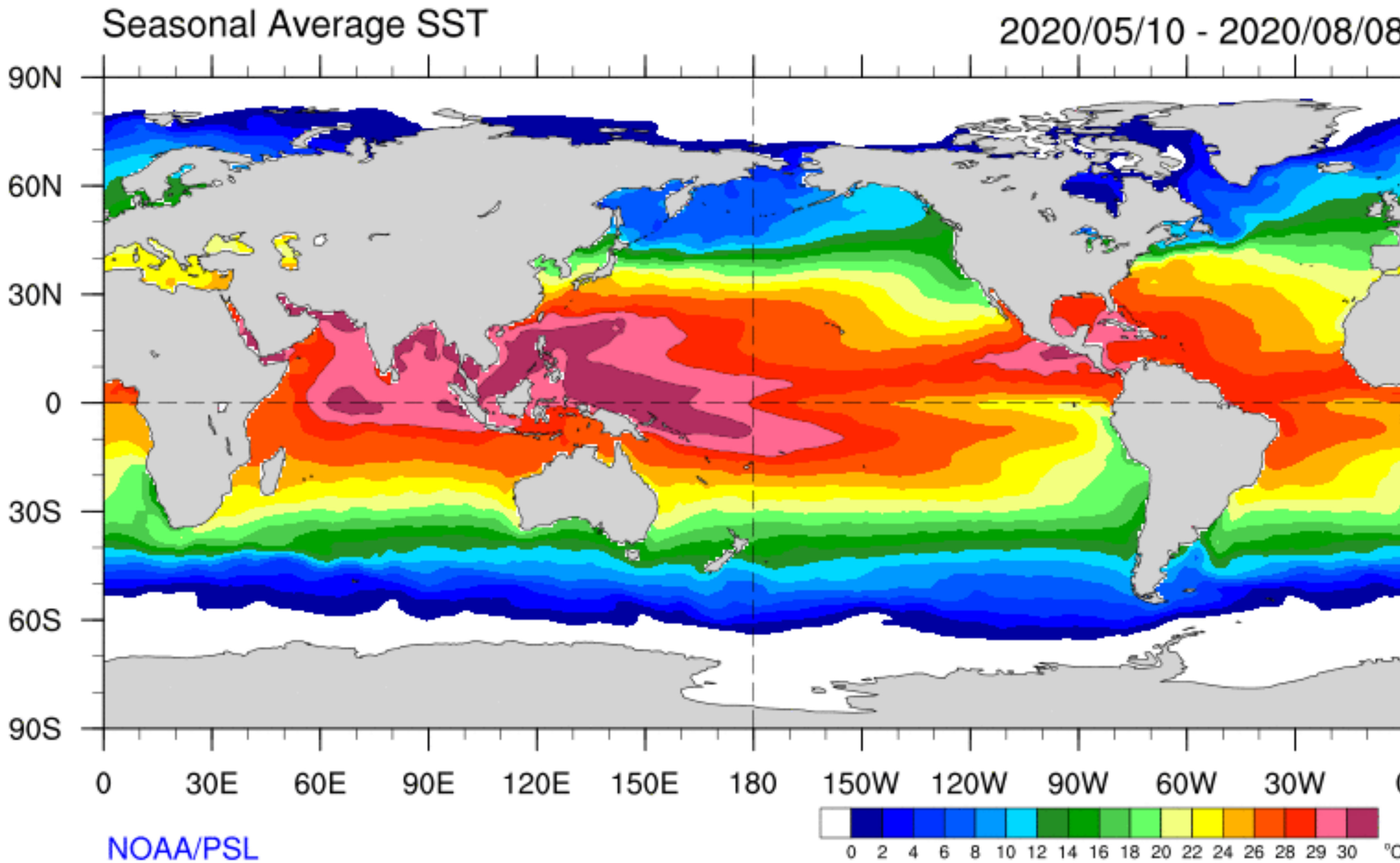

Seasonal Average SST
2020/05/10 - 2020/08/08
90N
60N
30N
0
30S
60S
90S
0
30E
60E
90E
120E
150E
180
150W
120W
90W
60W
30W
0
0
2
4
6
8
10
12
14
16
18
20
22
24
26
28
29
30
°C
NOAA/PSL

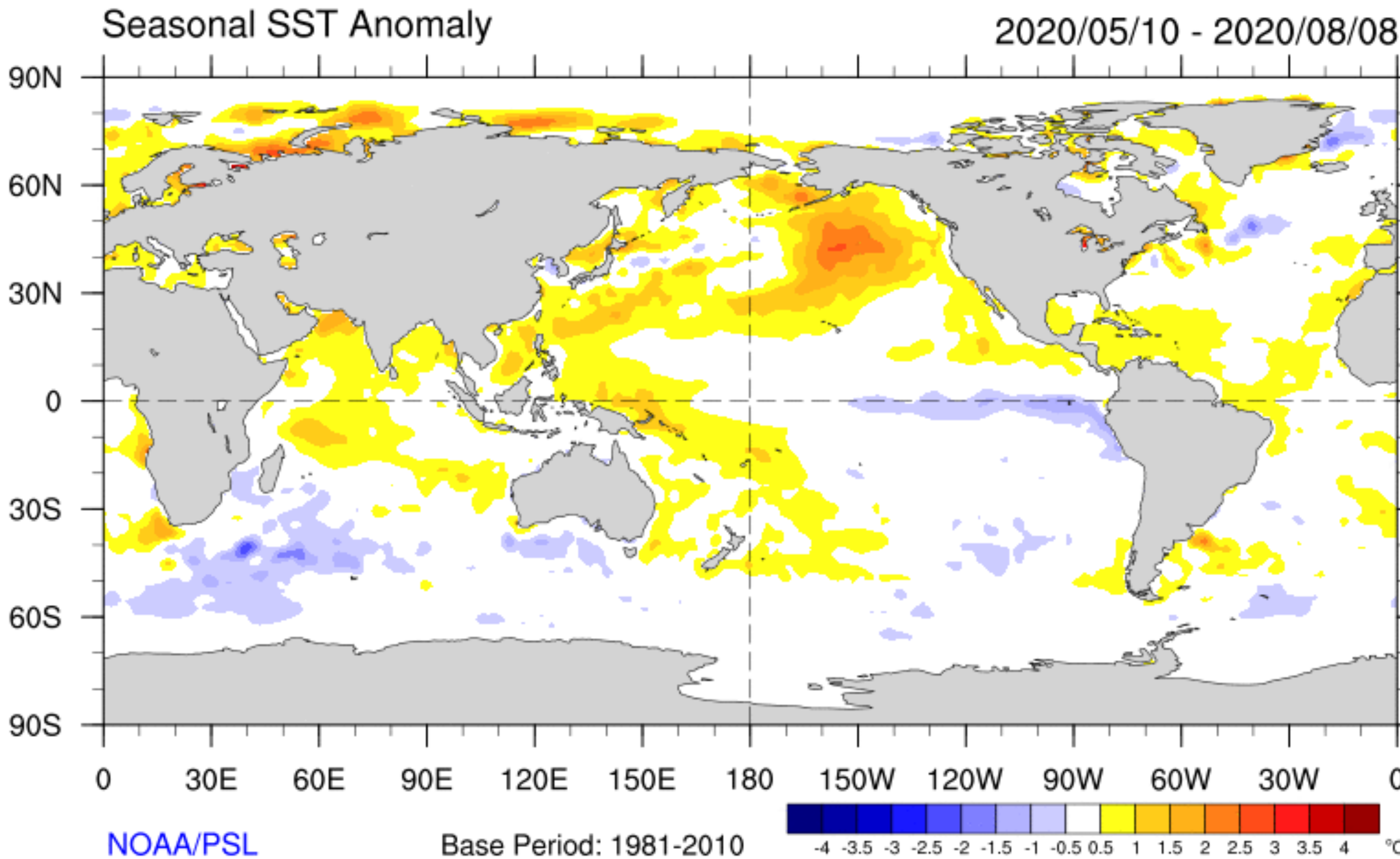
Seasonal SST Anomaly
2020/05/10 - 2020/08/08
90N
60N
30N
0
30S
60S
90S
0
30E
60E
90E
120E
150E
180
150W
120W
90W
60W
30W
0
NOAA/PSL
Base Period: 1981-2010
-4 -3.5 -3 -2.5 -2 -1.5 -1 -0.5 0.5 1 1.5 2 2.5 3 3.5 4
°C

Neutral ENSO

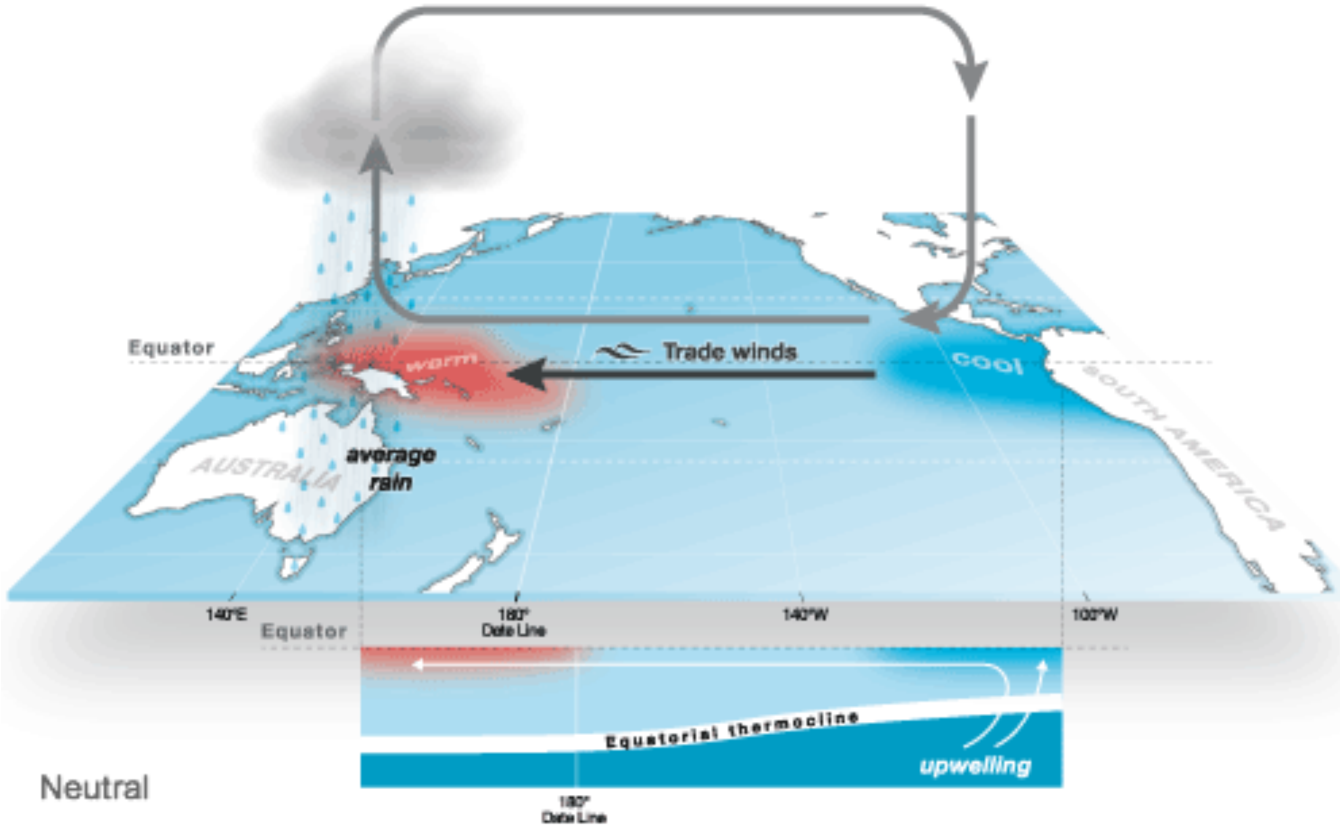

BoM Australia

La Niña

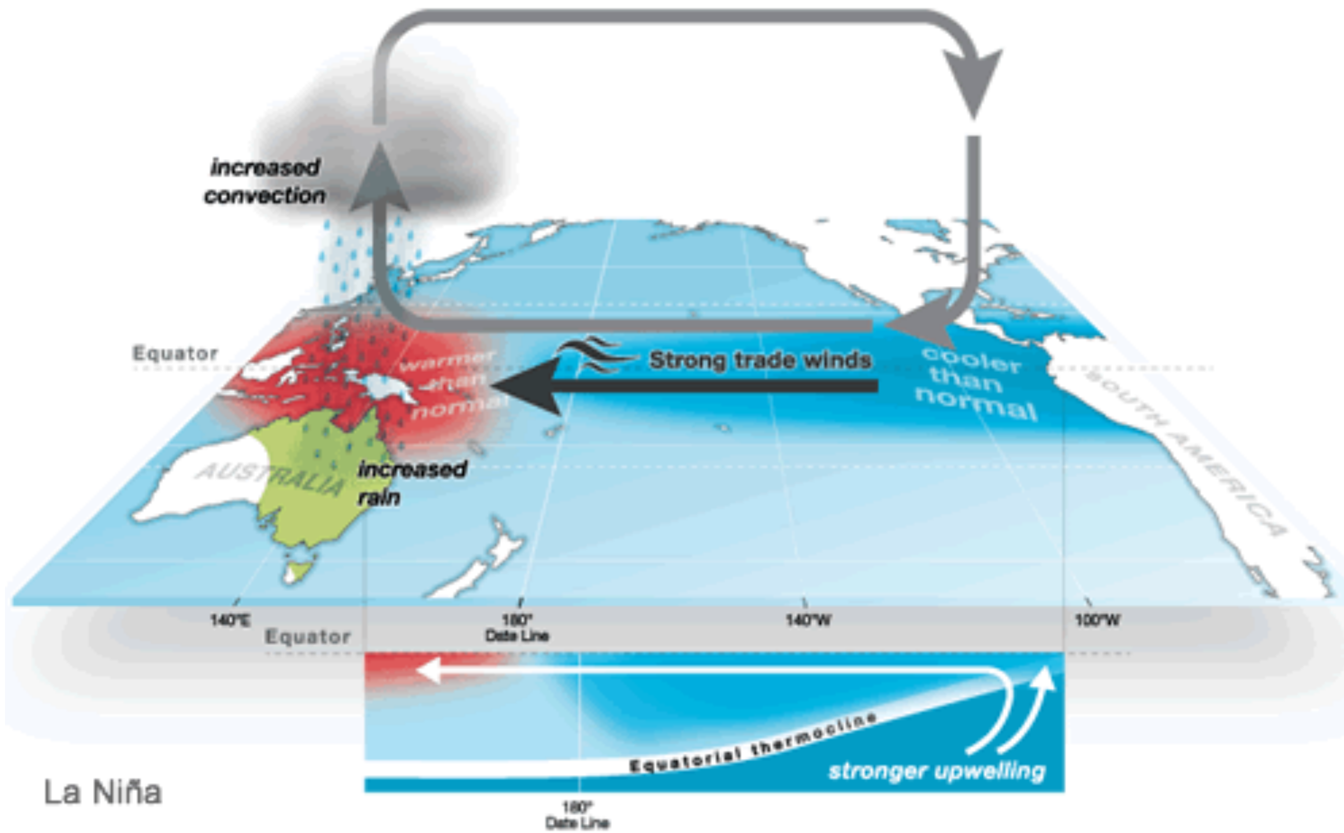

BoM Australia

El Niño

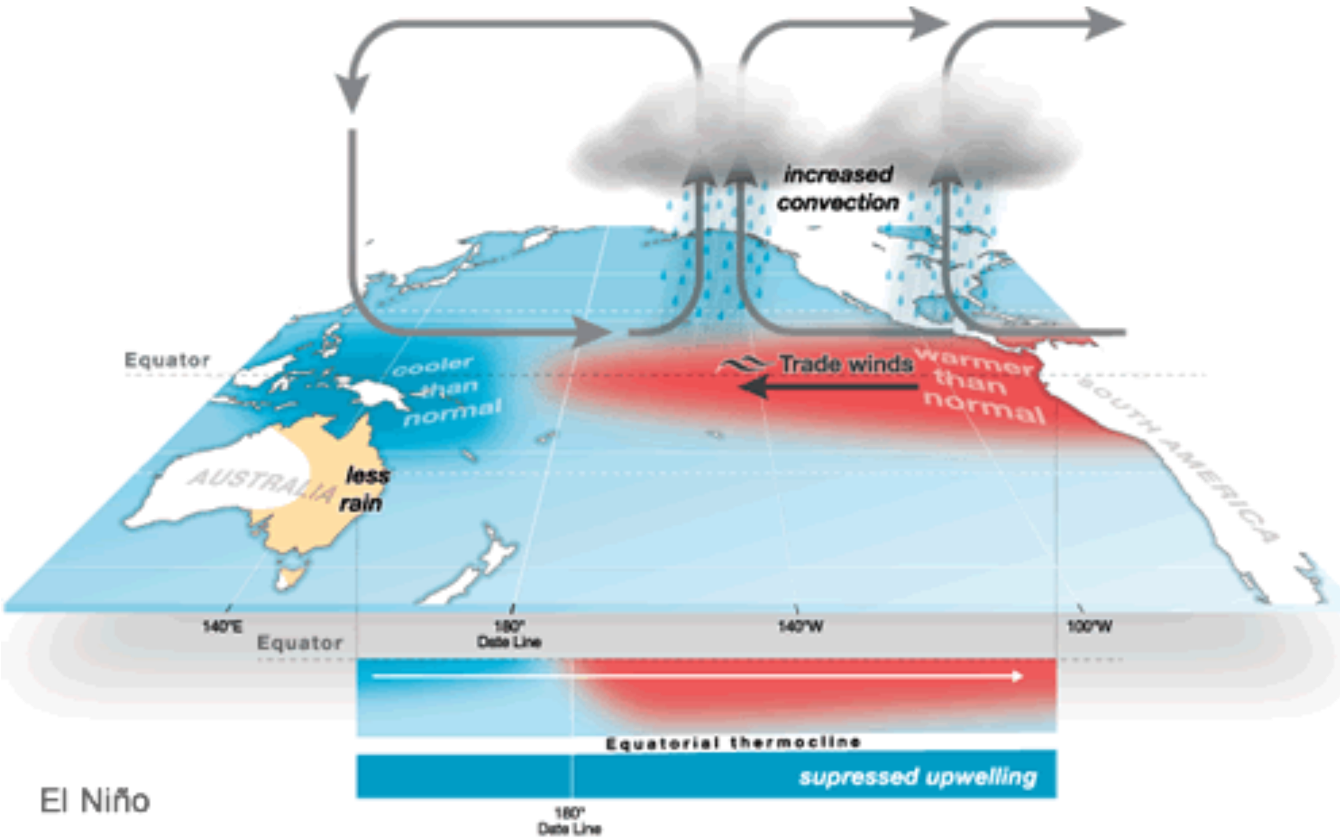

BoM Australia

1997 El Niño

NOAA

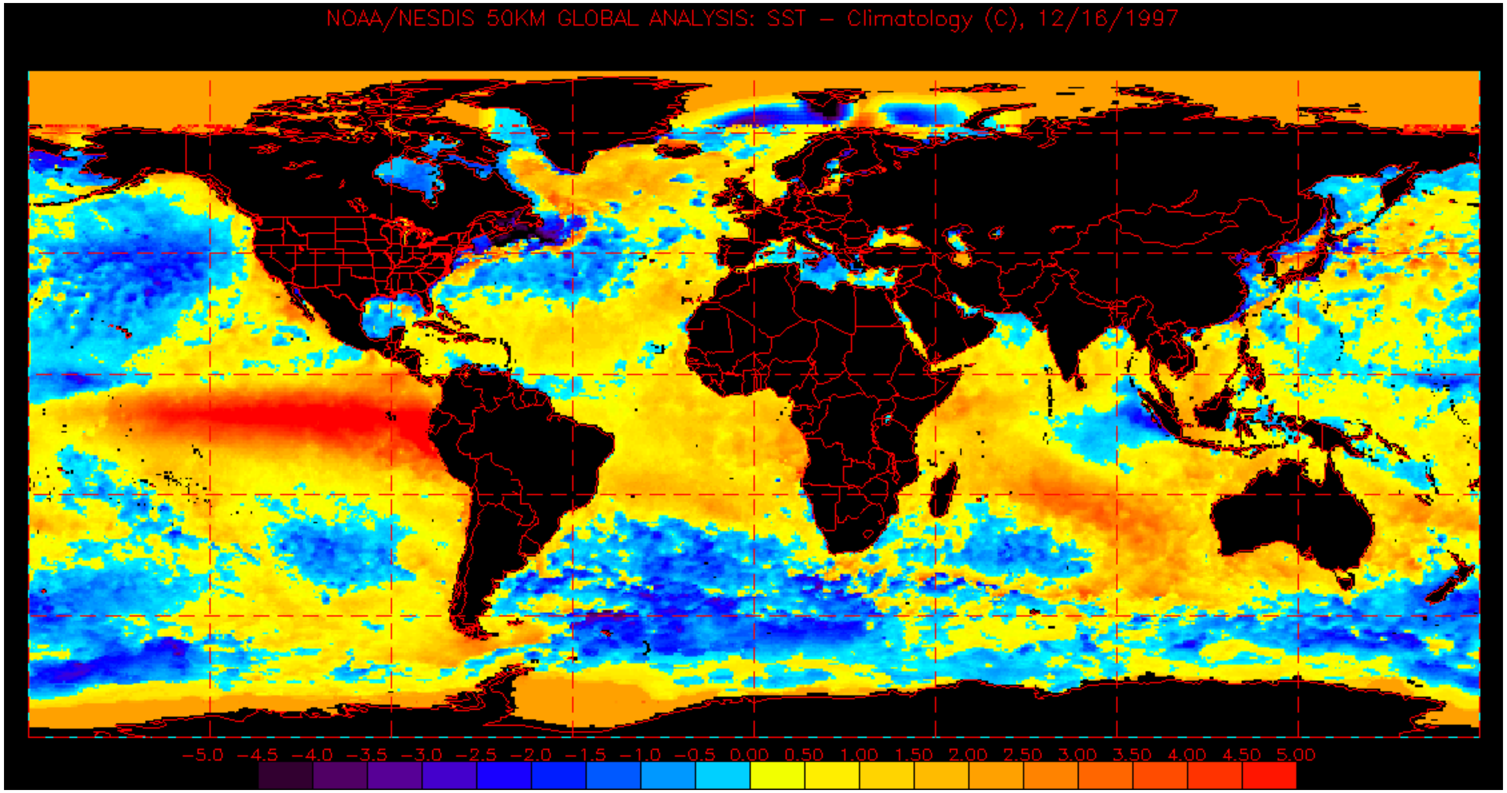

-5 -4 -3 -2 -1 0 +1 +2 +3 +4 +5

Temperature anomaly (°C)

1998 La Niña

NOAA

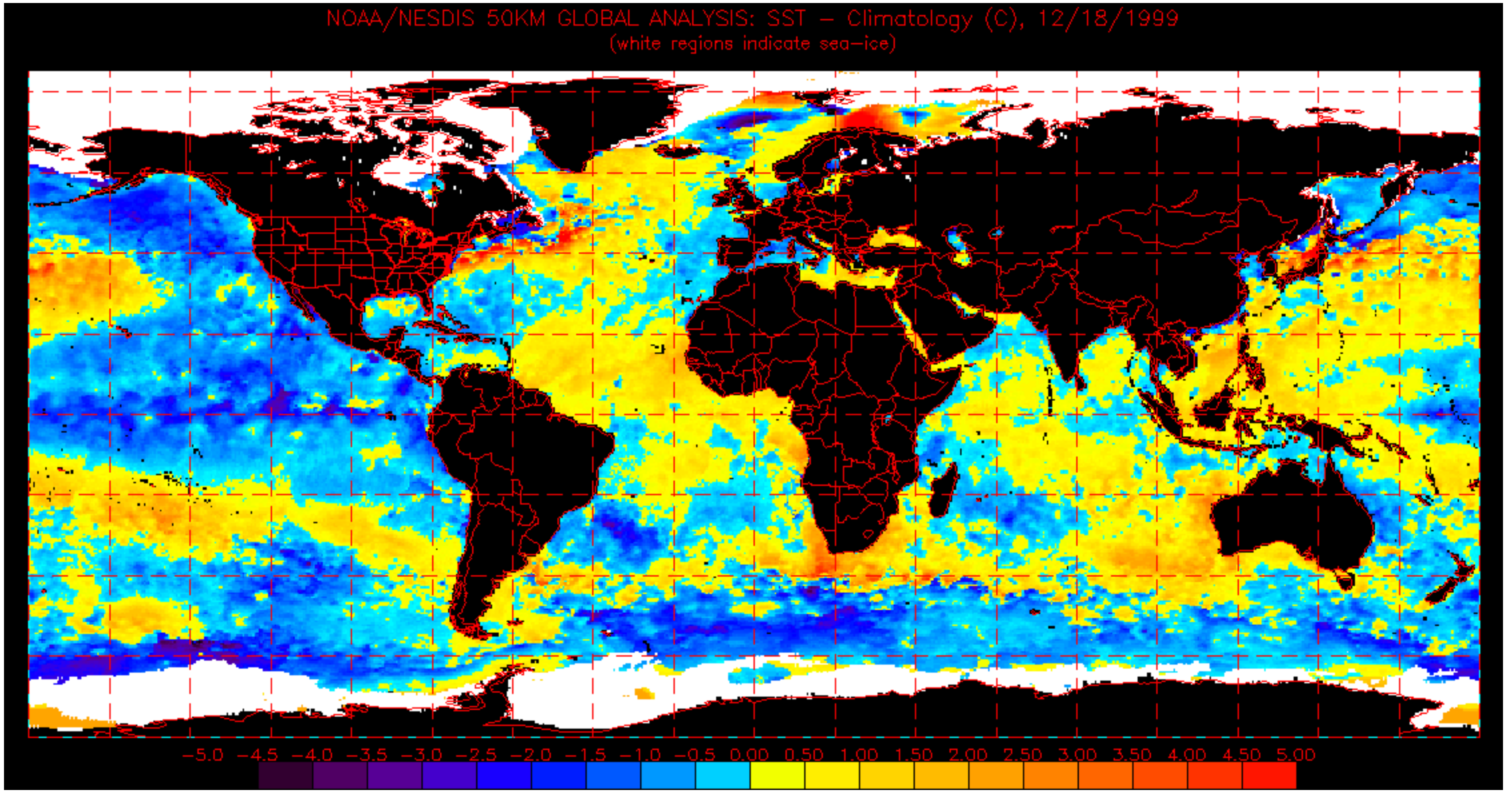

-5 -4 -3 -2 -1 0 +1 +2 +3 +4 +5

Temperature anomaly (°C)

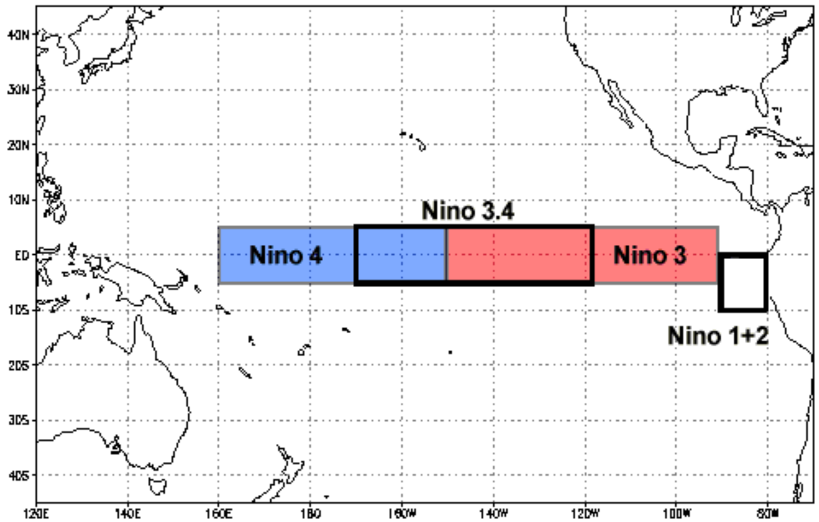

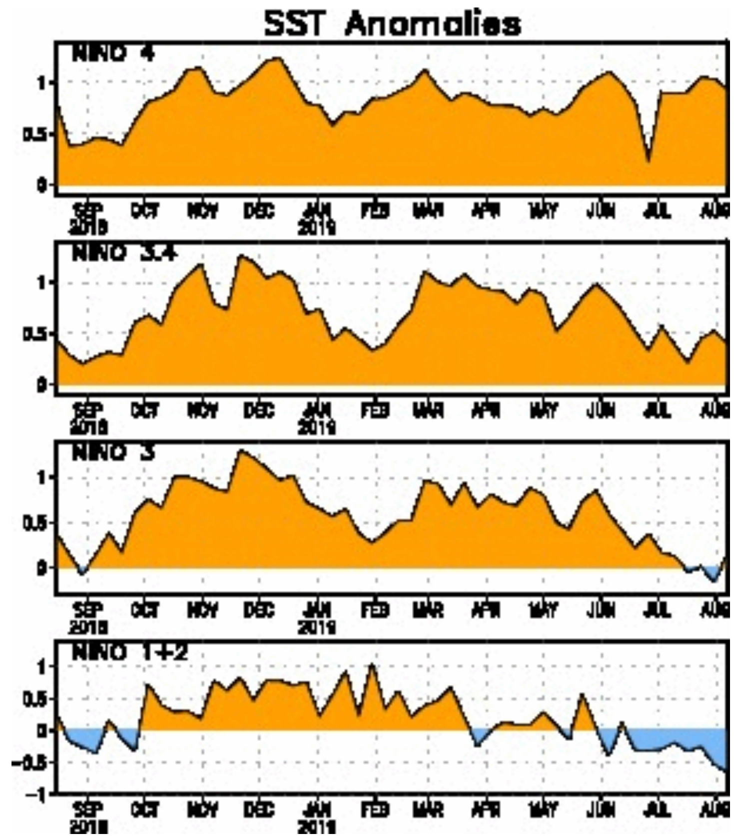

Other Indices: https://www.esrl.noaa.gov/psd/enso/dashboard.html

Indian Ocean Dipole

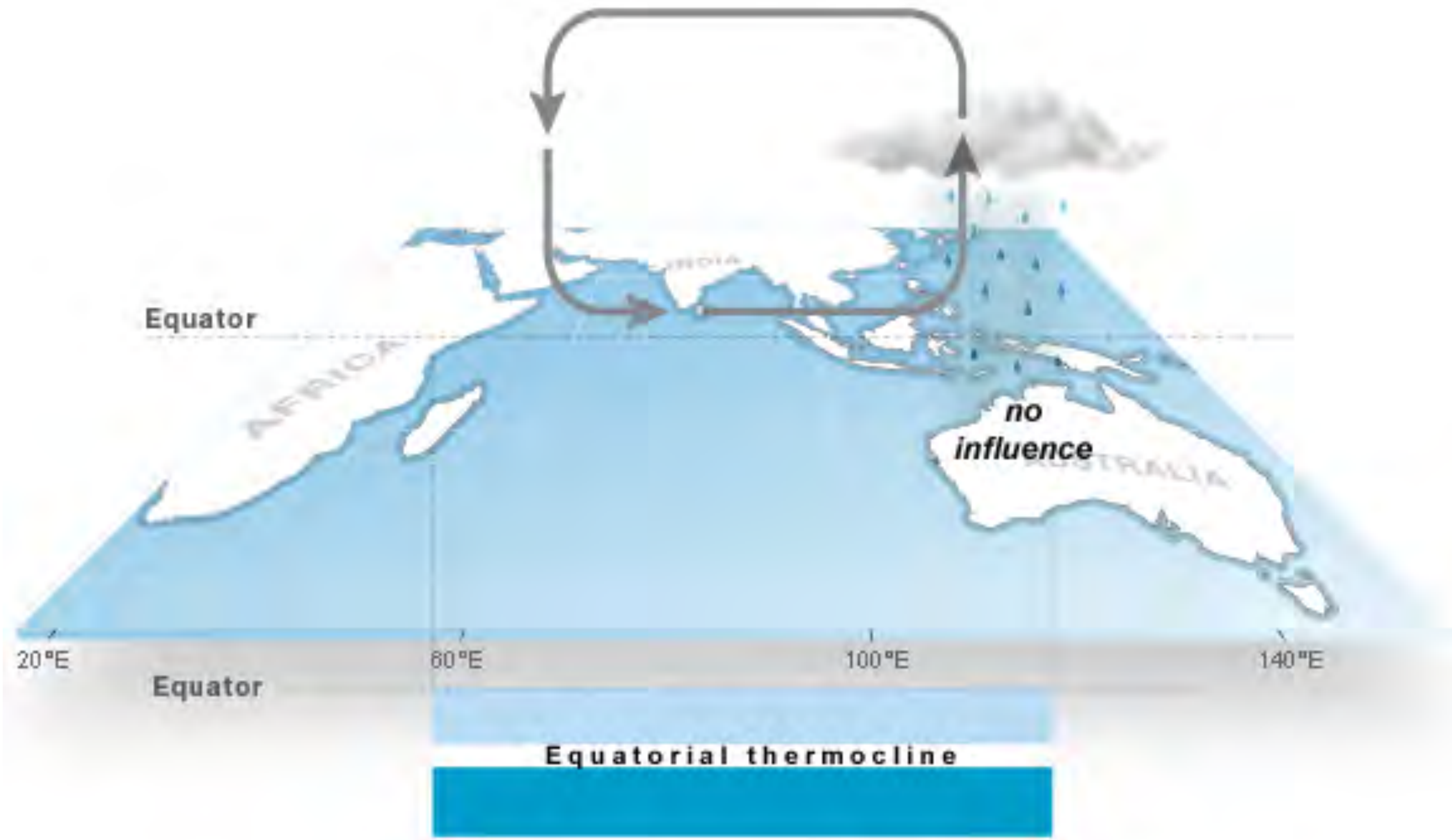

Indian Ocean Dipole (IOD): **Neutral phase**

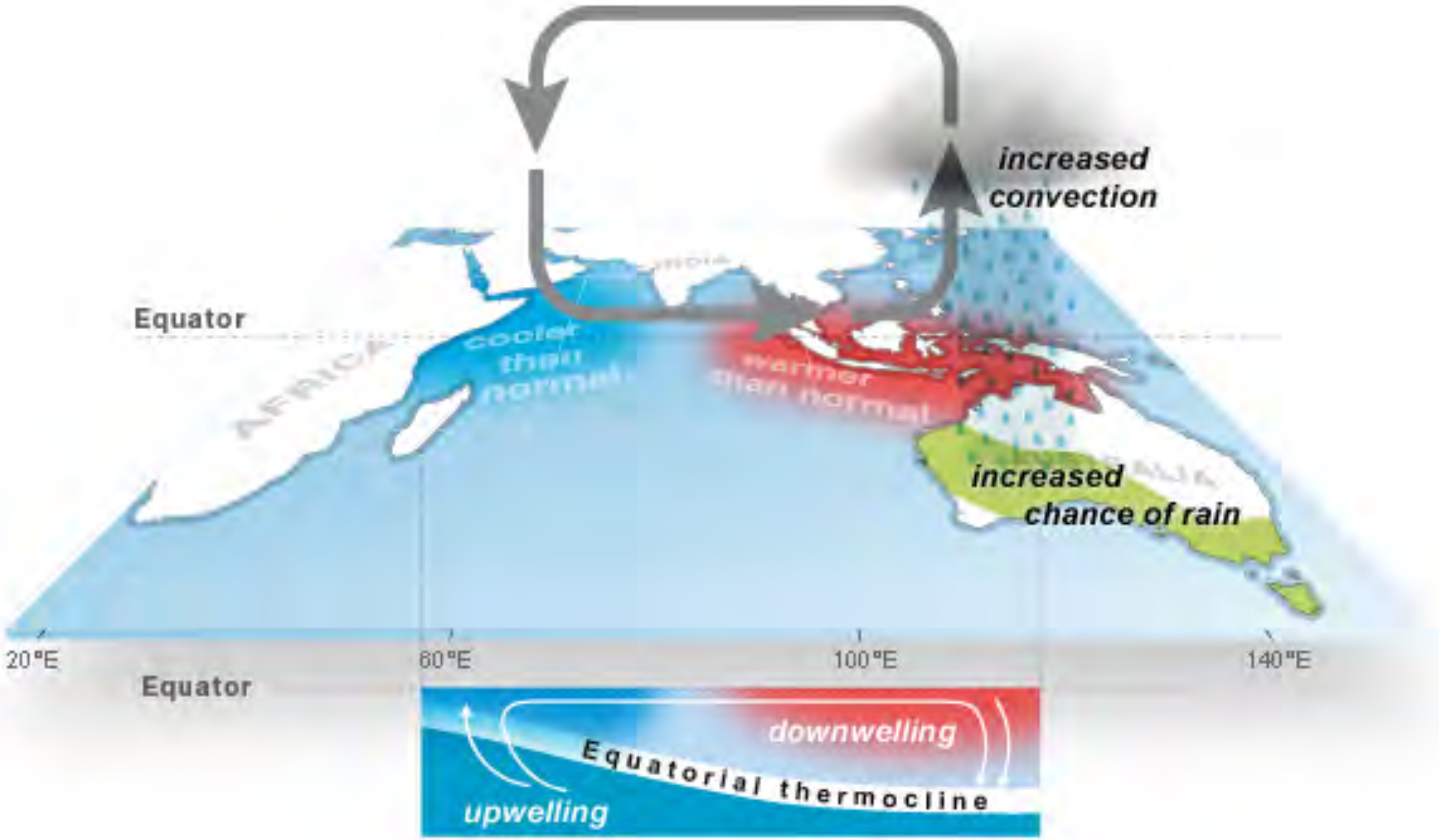

Indian Ocean Dipole (IOD): **Negative phase**

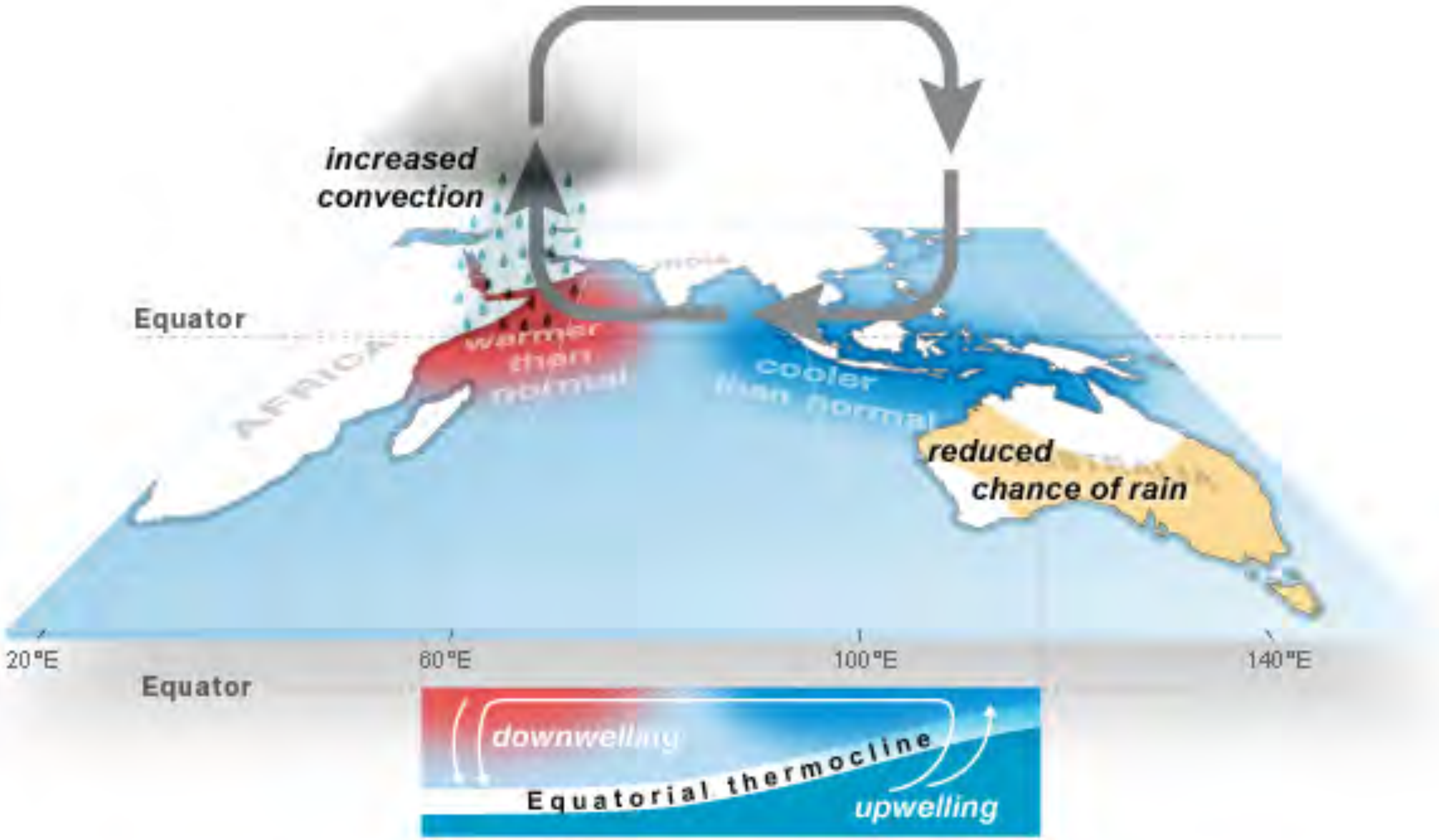

Indian Ocean Dipole (IOD): **Positive phase**

Strong positive Indian Ocean Dipole event, May–Dec 2019

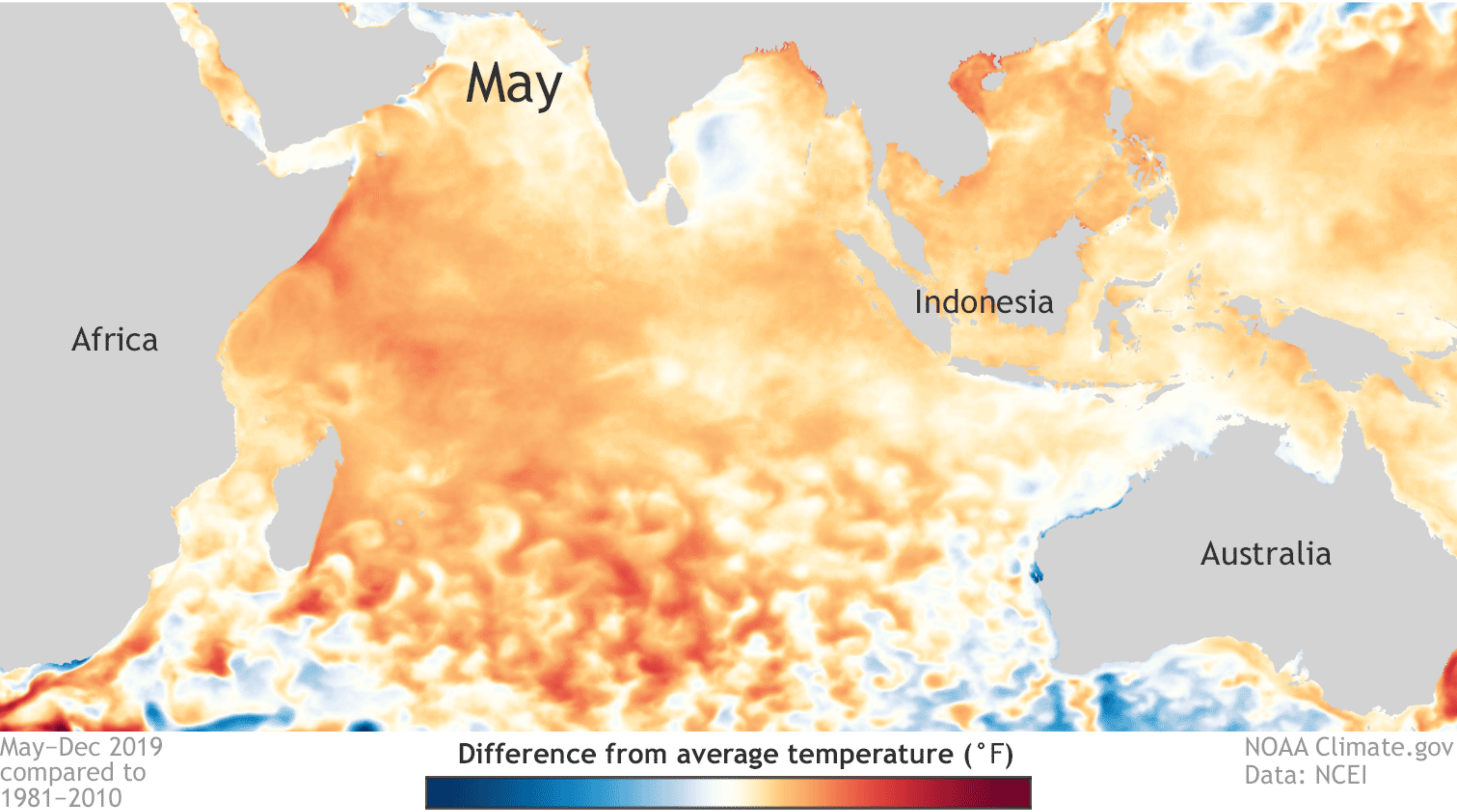

May–Dec 2019
compared to
1981–2010

NOAA Climate.gov
Data: NCEI

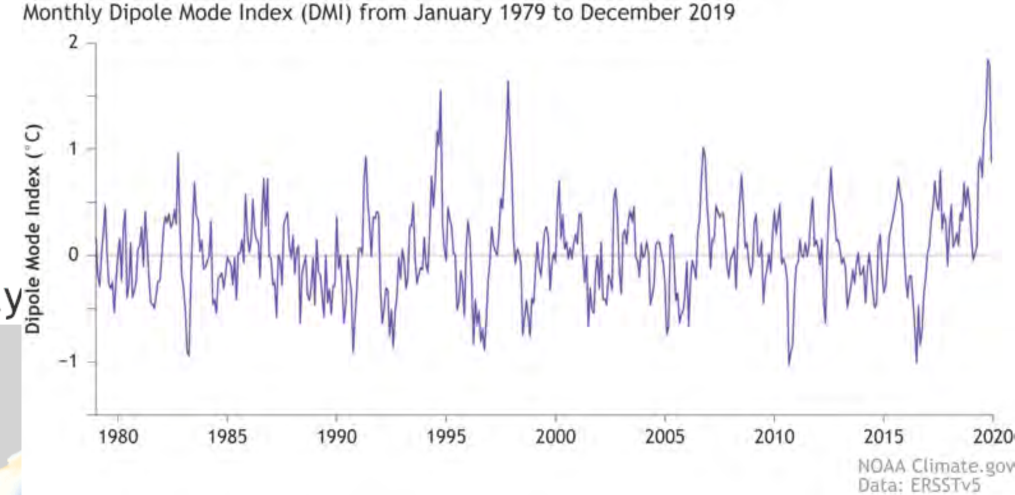

Strong positive Indian Ocean Dipole event, May

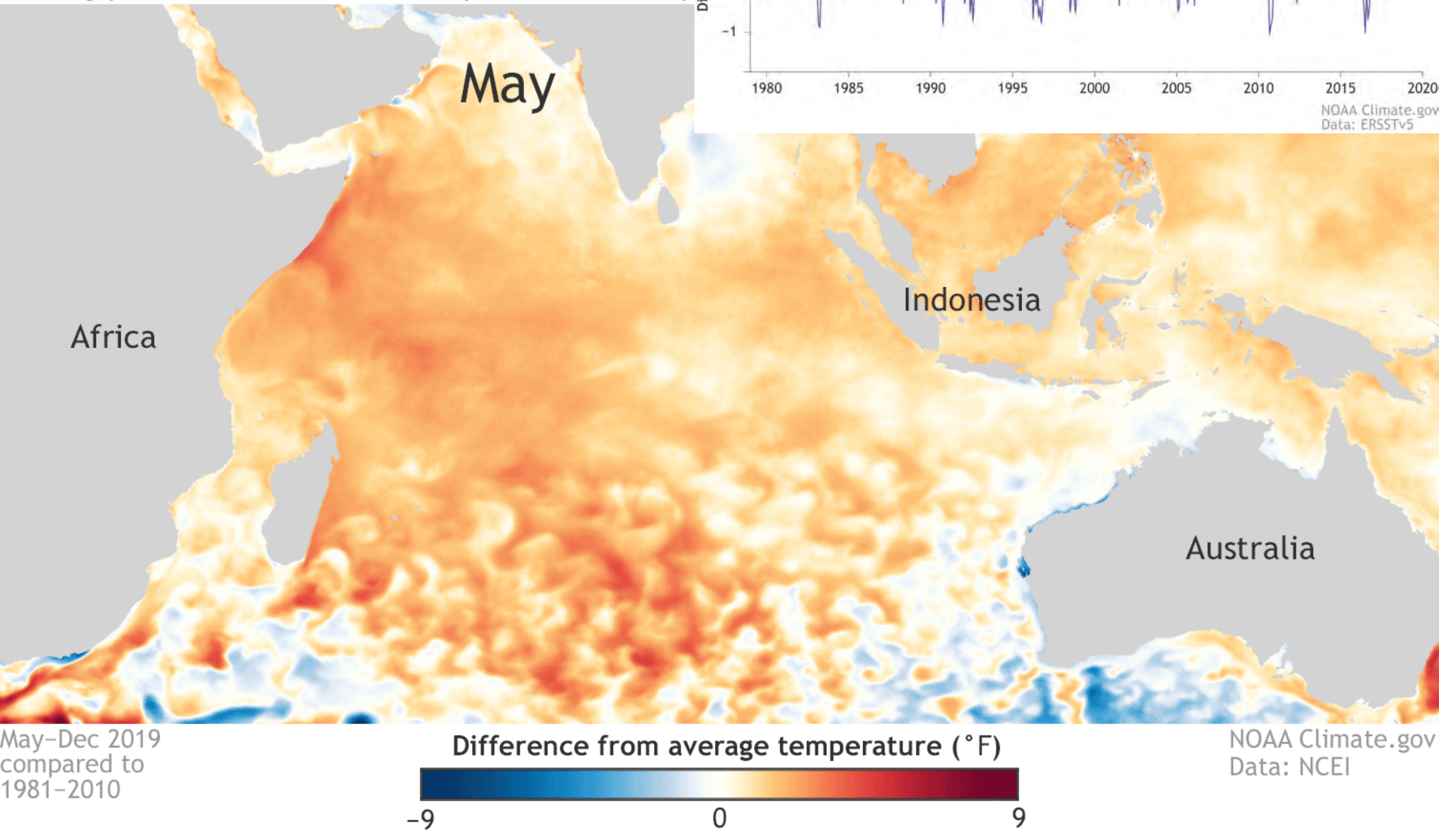

MR3252: Tropical Meteorology

Monsoons

Main Topics:

- Asian-Australian monsoon
- Monsoon depressions
- Enhanced precipitation along small topographical features

Module 4.3

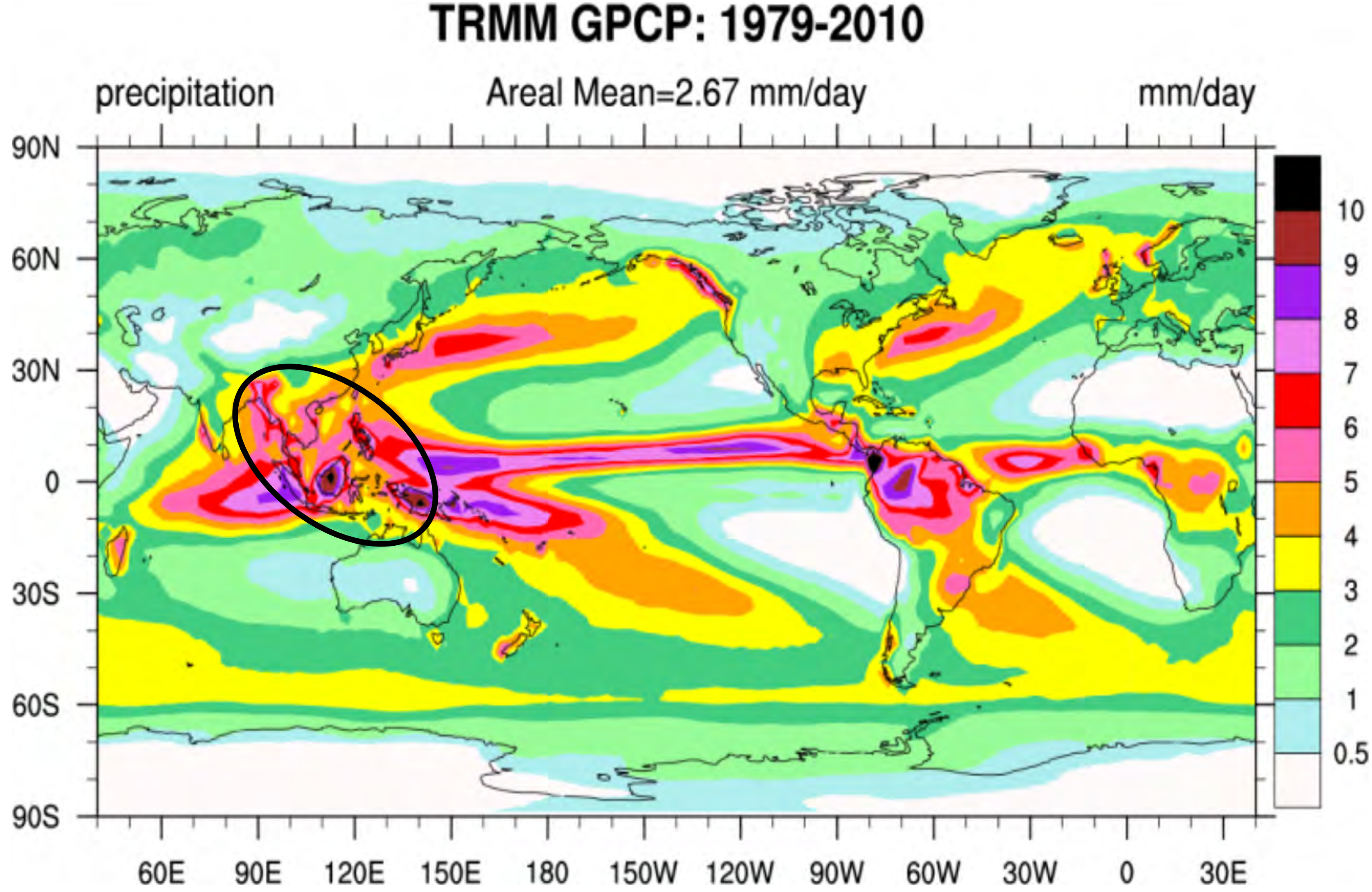
TRMM GPCP: 1979-2010
precipitation
Areal Mean=2.67 mm/day
mm/day
90N
60N
30N
0
30S
60S
90S
60E
90E
120E
150E
180
150W
120W
90W
60W
30W
0
30E
10
9
8
7
6
5
4
3
2
1
0.5

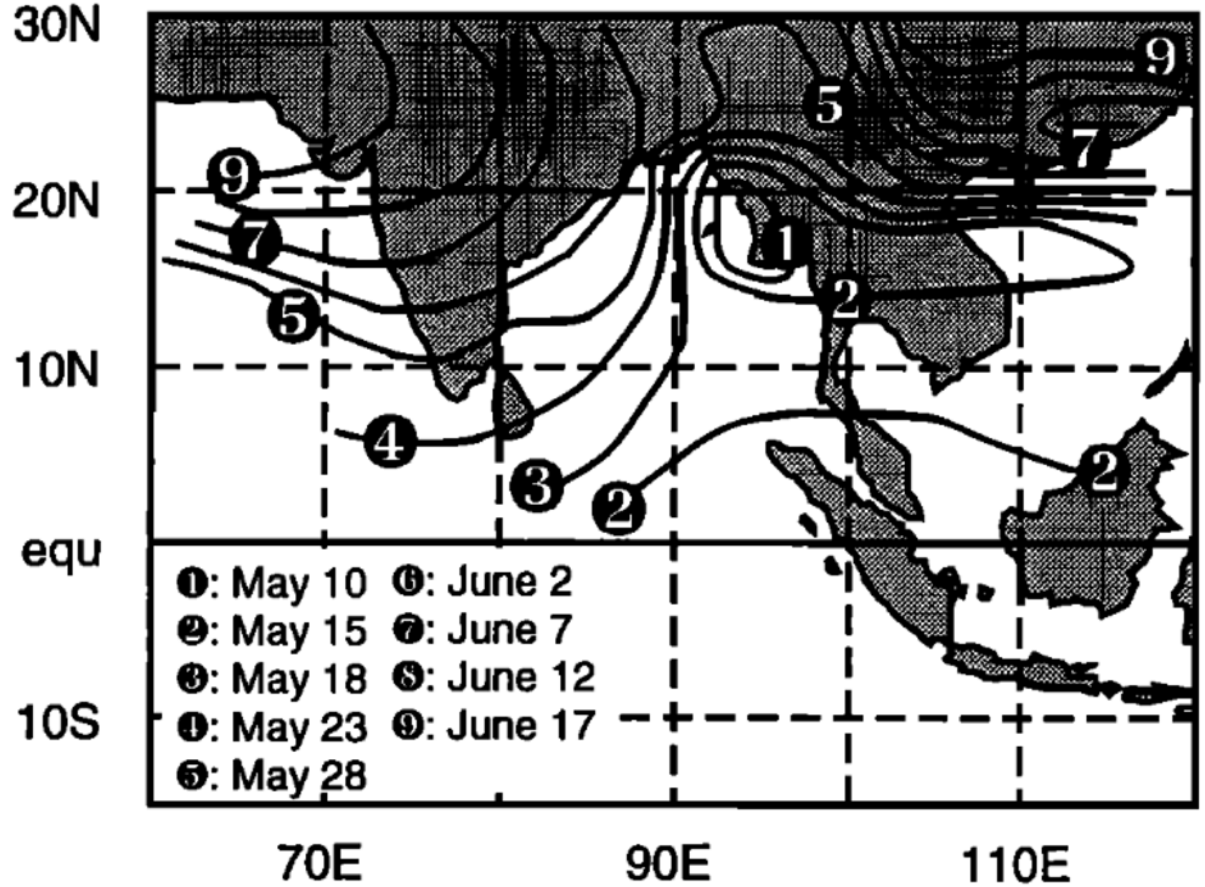

Figure 13a. Climatological times of the onset of the south Asian summer monsoon based on the mean positions of the 220 W m^{-2} outgoing longwave radiation from 1980–1992.

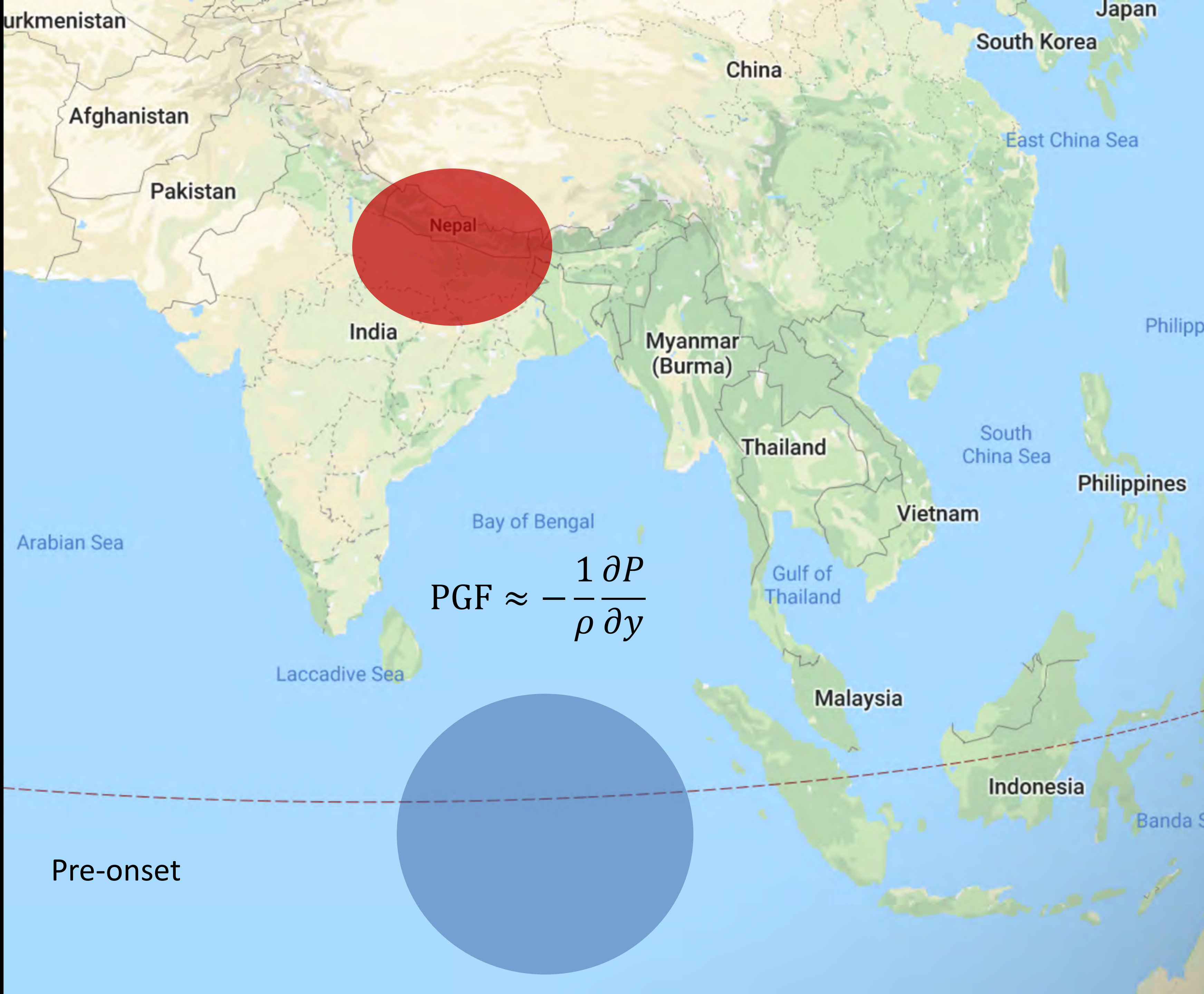

$$\text{PGF} \approx -\frac{1}{\rho}\frac{\partial P}{\partial y}$$

Pre-onset

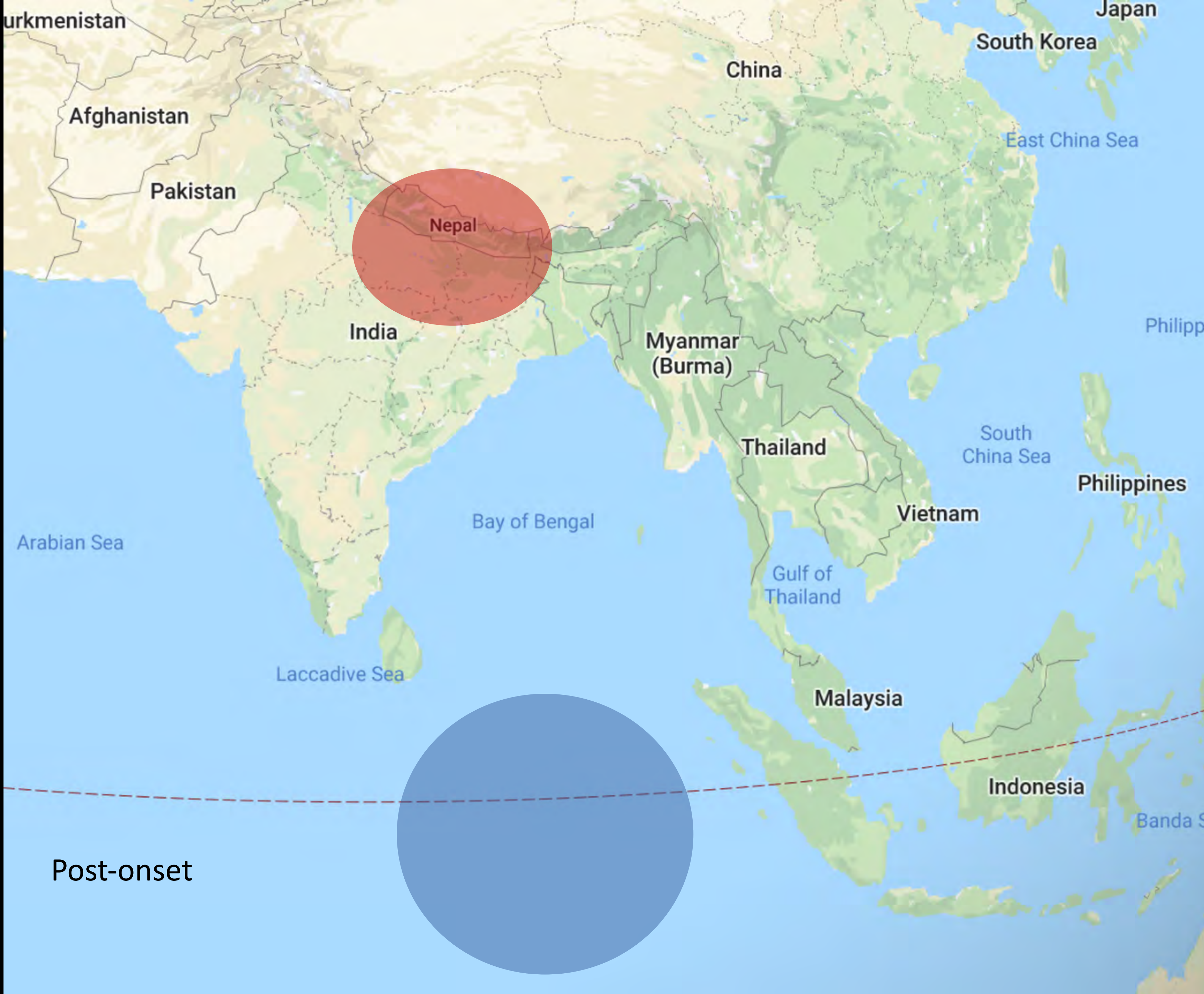
urkmenistan
Japan
South Korea
China
Afghanistan
East China Sea
Pakistan
Nepal
India
Myanmar
(Burma)
Philippi
South
China Sea
Thailand
Philippines
Vietnam
Bay of Bengal
Arabian Sea
Gulf of
Thailand
Laccadive Sea
Malaysia
Indonesia
Banda Se
Post-onset

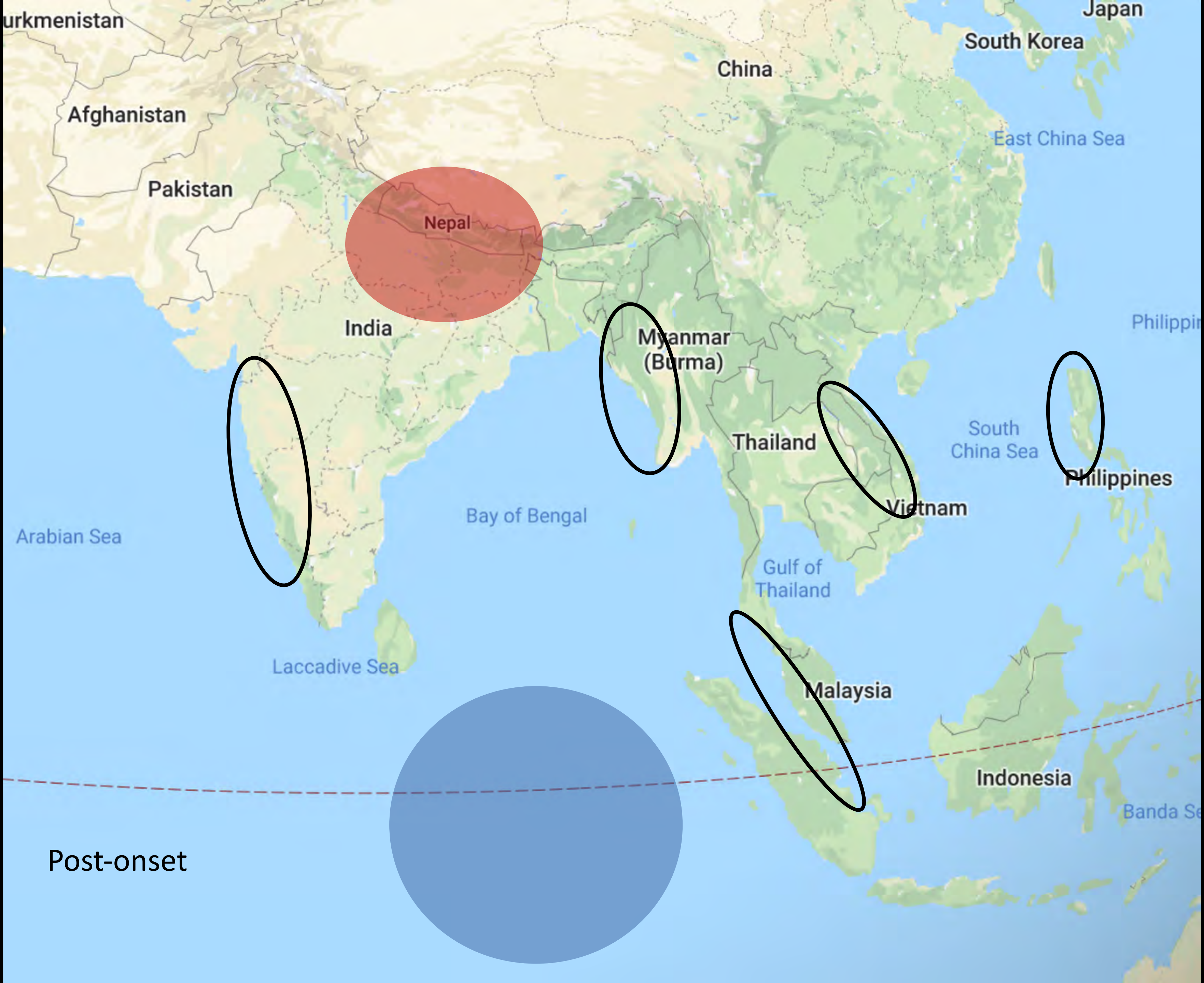
urkmenistan
Japan
South Korea
China
Afghanistan
East China Sea
Pakistan
Nepal
India
Myanmar
(Burma)
Philippi
South
China Sea
Thailand
Philippines
Vietnam
Bay of Bengal
Arabian Sea
Gulf of
Thailand
Laccadive Sea
Malaysia
Indonesia
Banda Se
Post-onset

200-500 mb Temperature

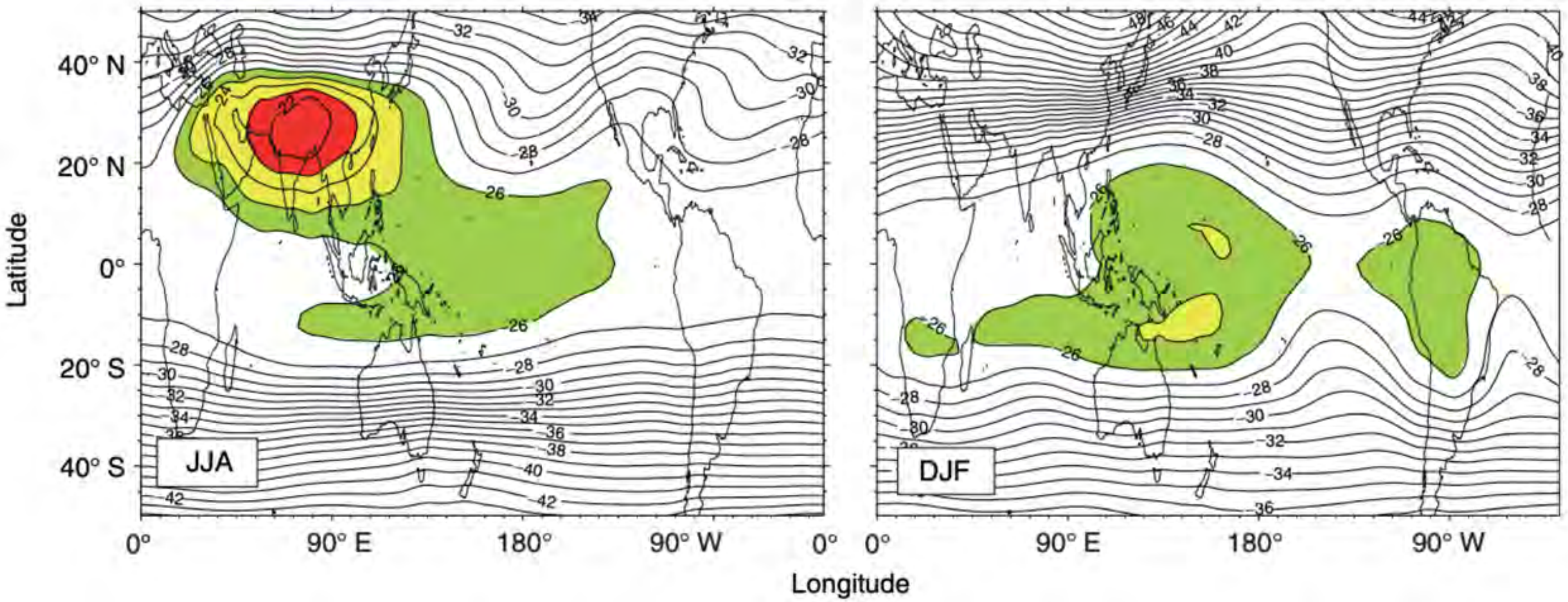

Figure 7 Distribution of the mean upper tropospheric temperature averaged between 200 and 500 hPa for the boreal summer (JJA) and winter (DJF). Note the two locations where the mean temperature is warmer than the equatorial temperature: over the Tibetan Plateau during the boreal summer and to the north-east of Australia in the austral summer.

Webster and Fasullo (2003)

South Asian Summer Monsoon

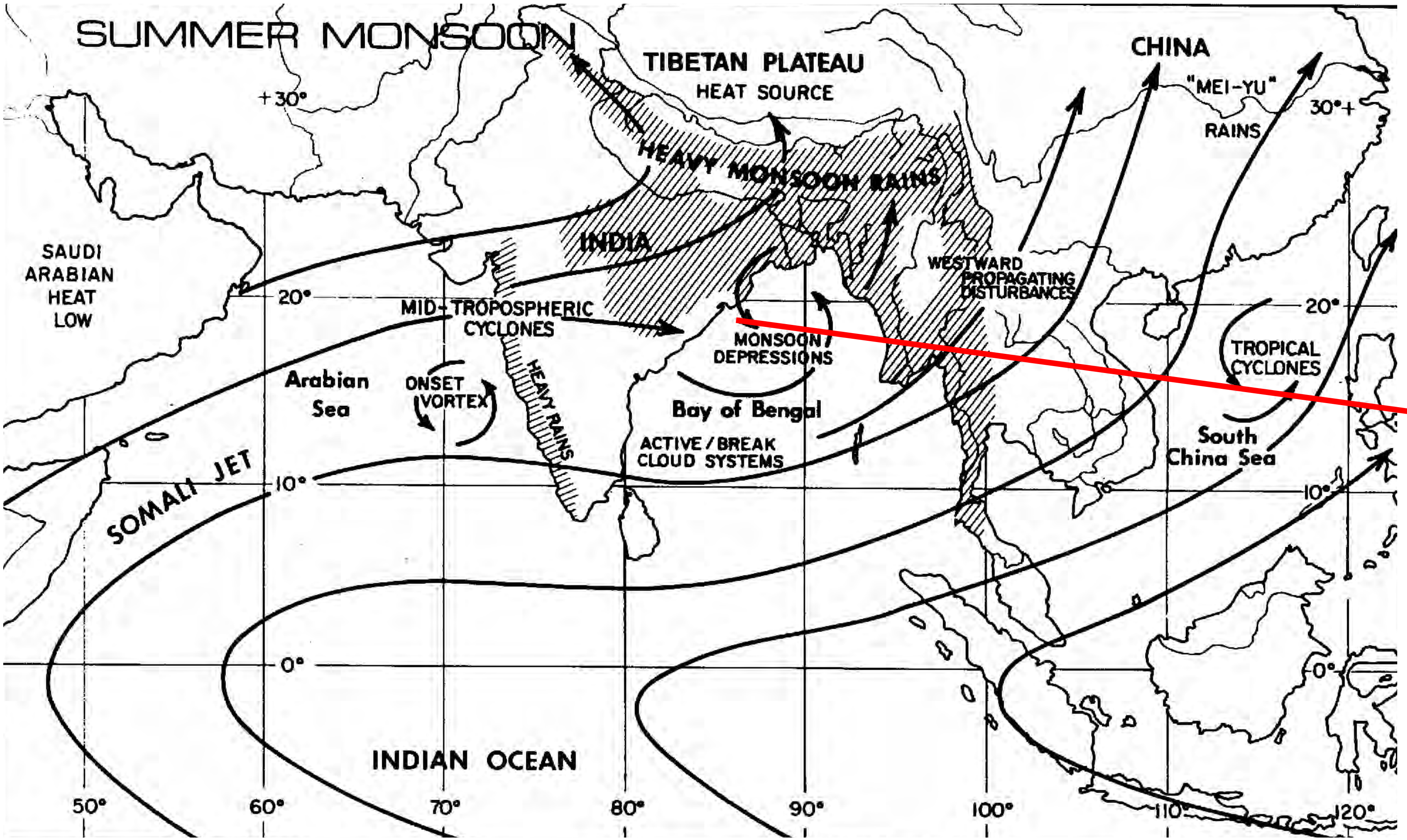

Summer monsoon

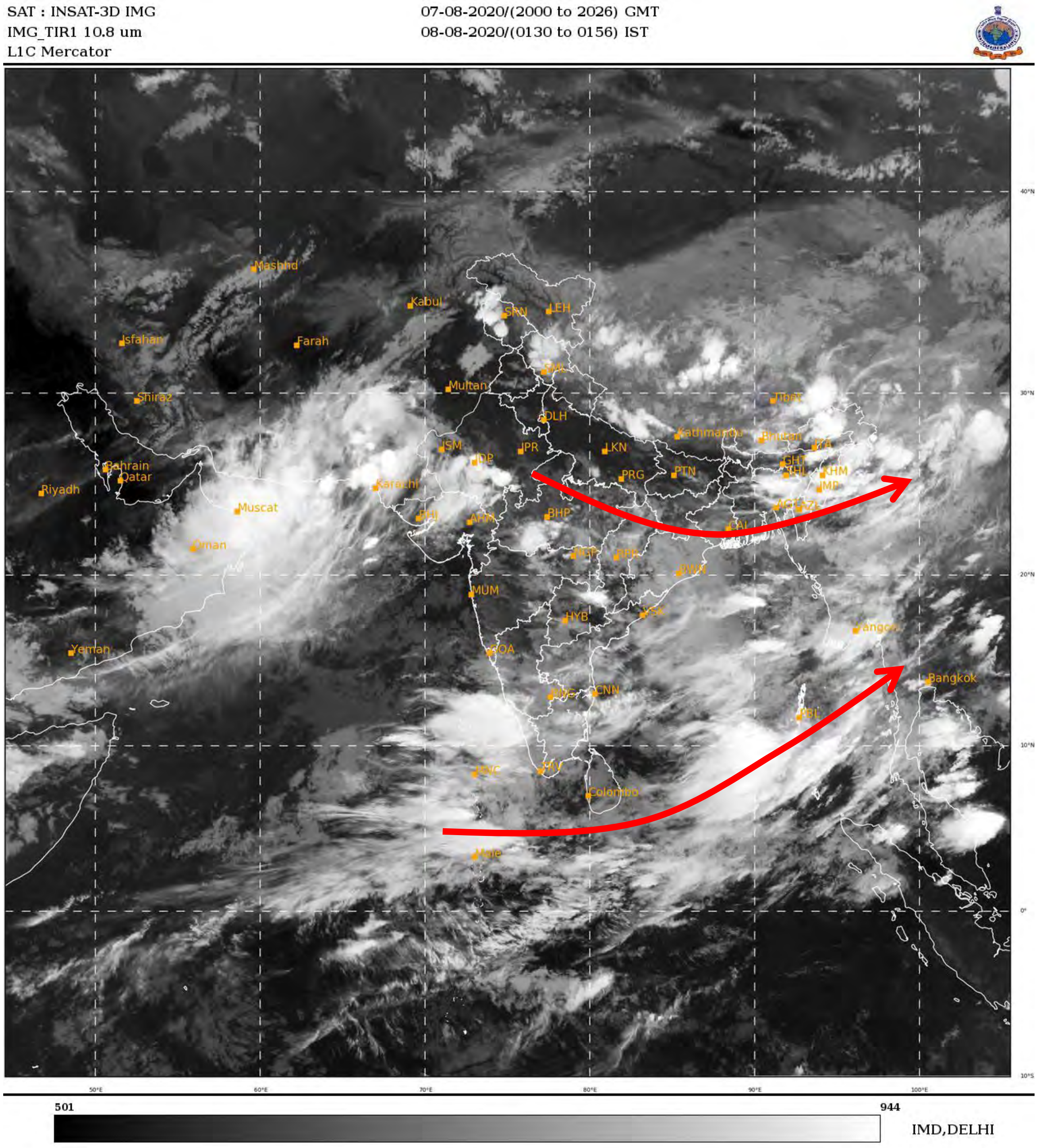

Fletcher et al. (2019)

Western Ghats

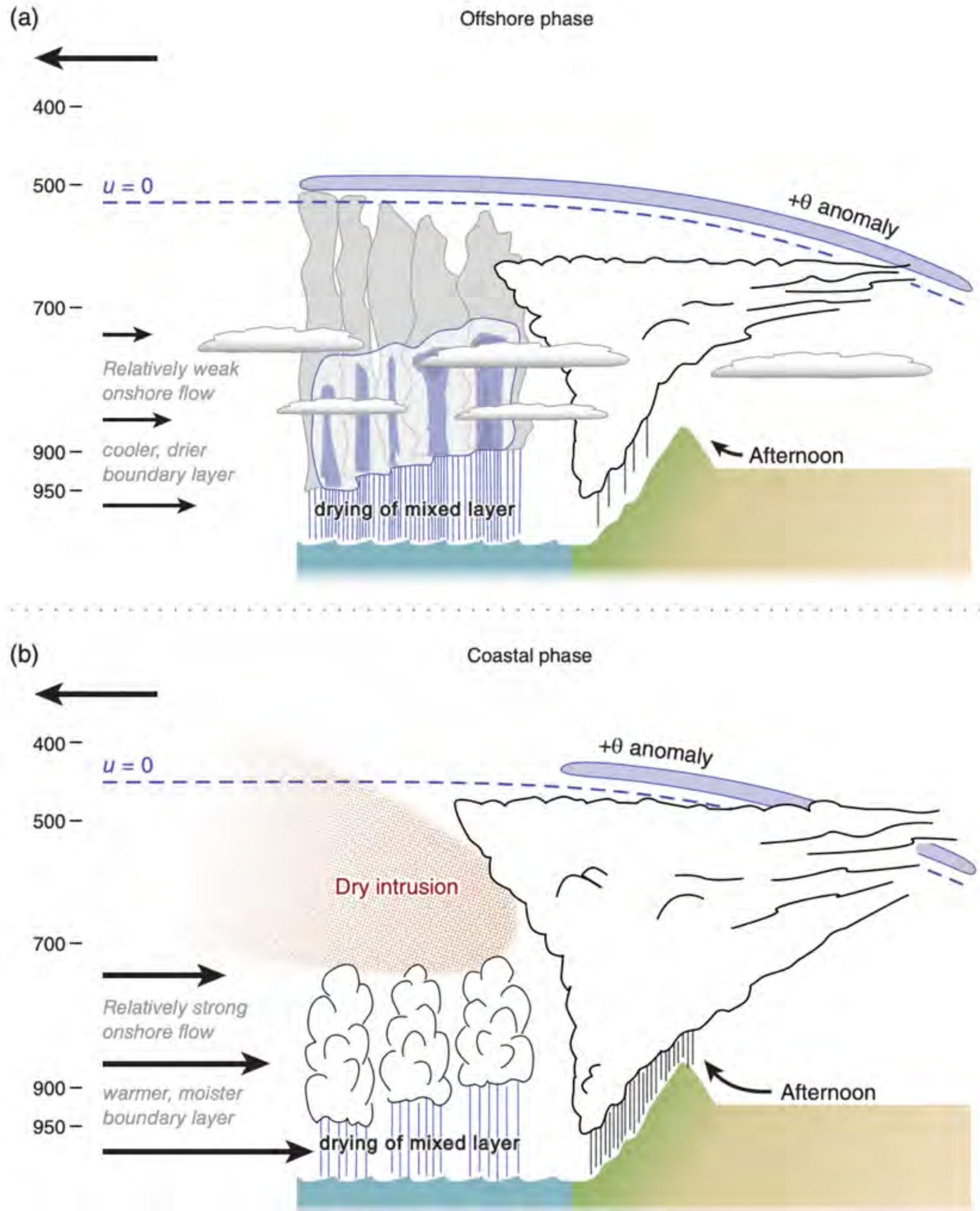

FIGURE 15 Schematic of the most important features of (a) the offshore phase and (b) the coastal phase. Section 7 gives discussion. Art by Beth Tully [Colour figure can be viewed at wileyonlinelibrary.com]

Monsoon Depressions

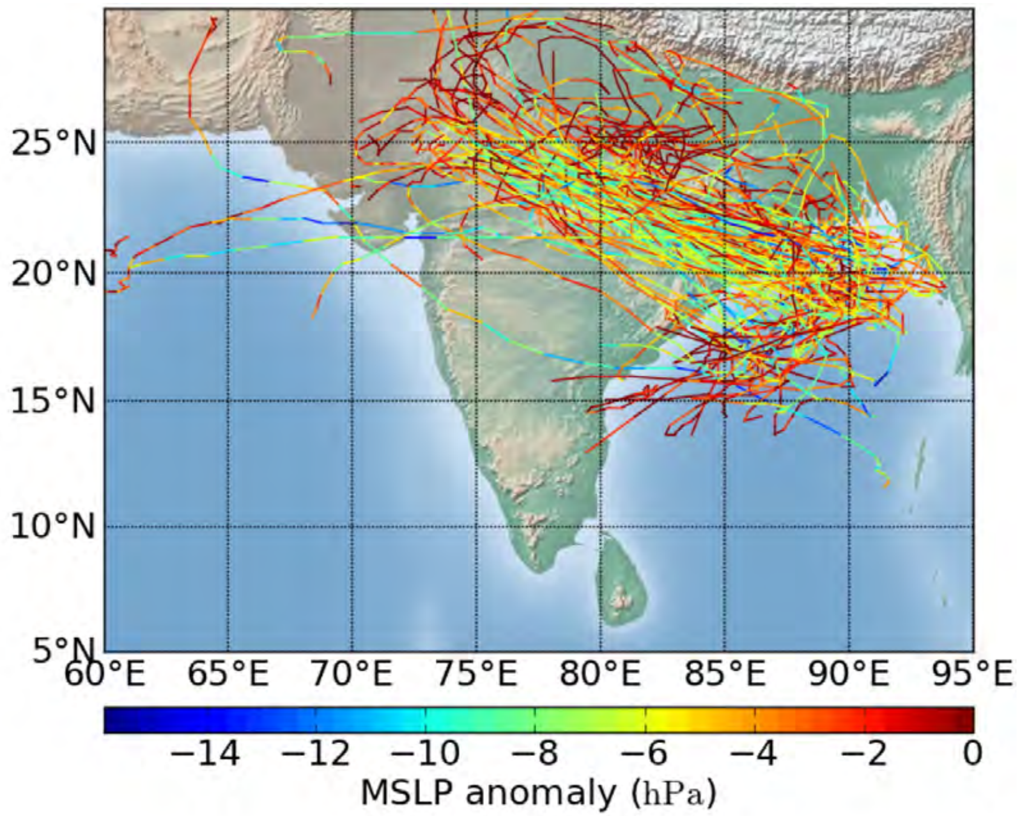

(b)

Hunt et al. (2016; MWR)

What causes these to move northwestward?
Beta drift? (Boos et al. 2015)
Cloud-radiative feedback amplification? (Adames and Ming 2018)

Austral-Asian Monsoon

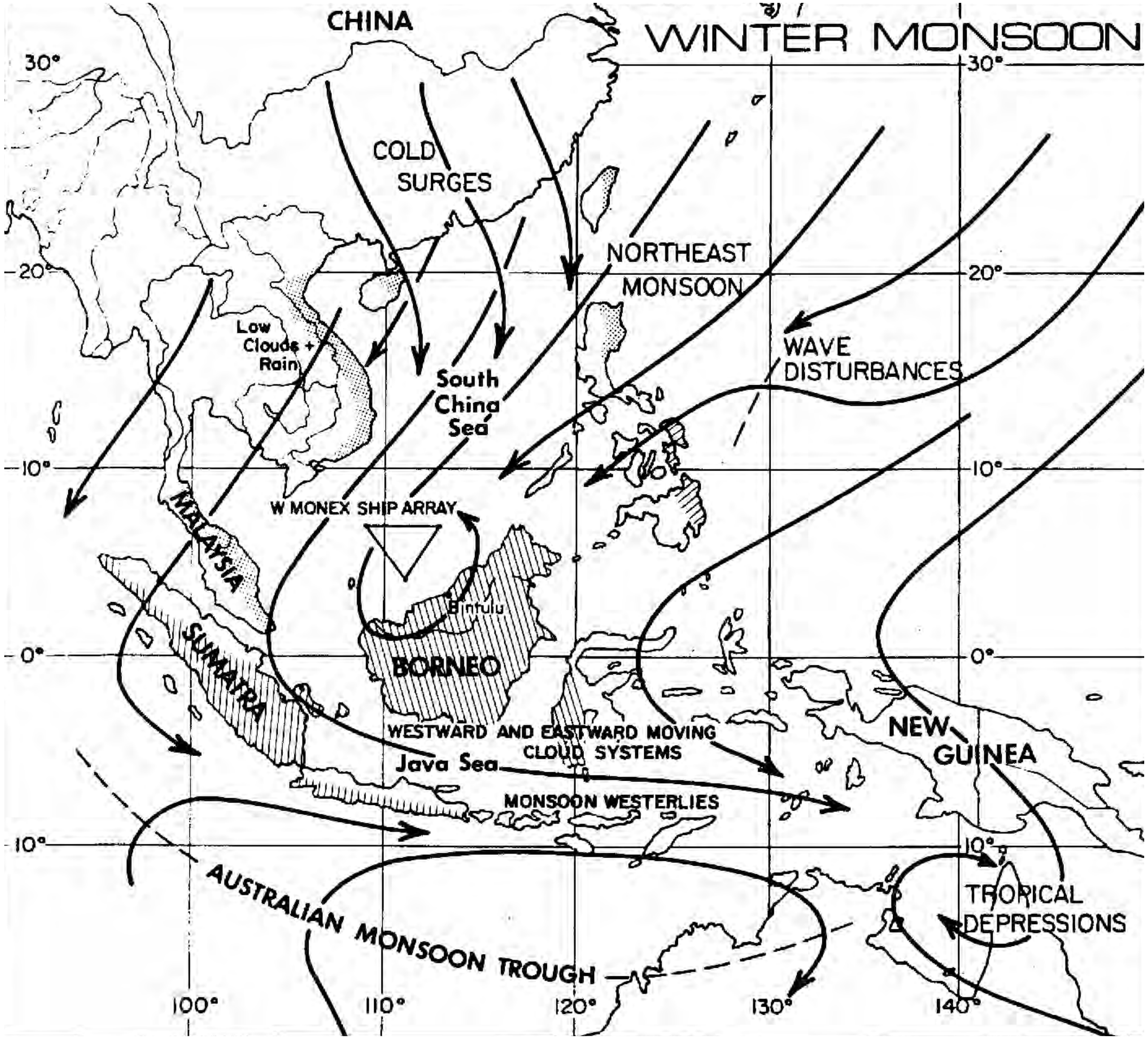

NASA video showing satellite data during various monsoons:

https://svs.gsfc.nasa.gov/12303

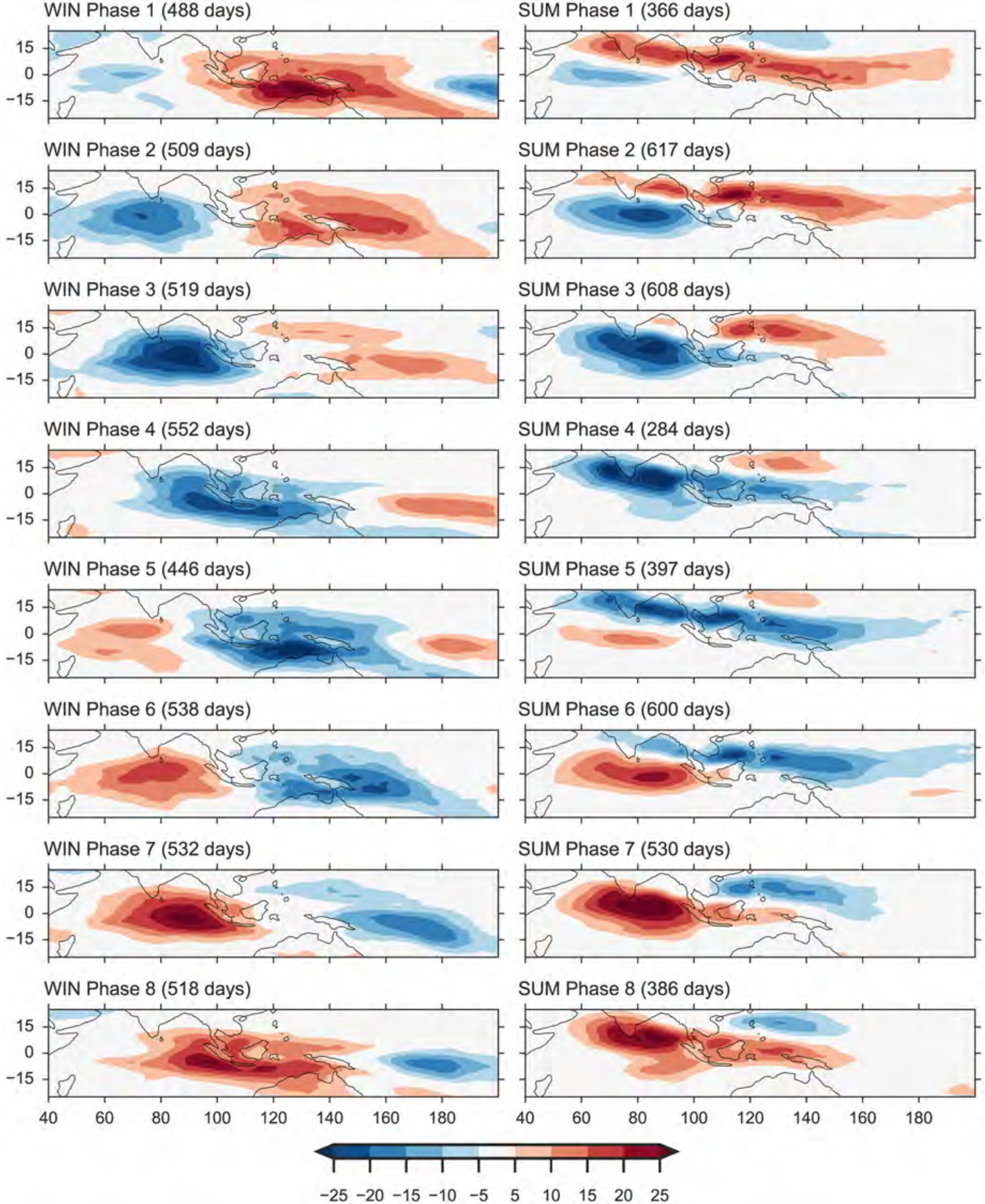

Wang et al. (2018)

Intraseasonal variability in monsoon precipitation over SE Asia

MR3252: Tropical Meteorology

Mid-Latitude Dynamics Forced by Tropical Convection

Main Topics:

- ENSO ″teleconnections″
- Mid-latitude examples of sub-seasonal variability
- Extratropical response to tropical heating

Module 4.4

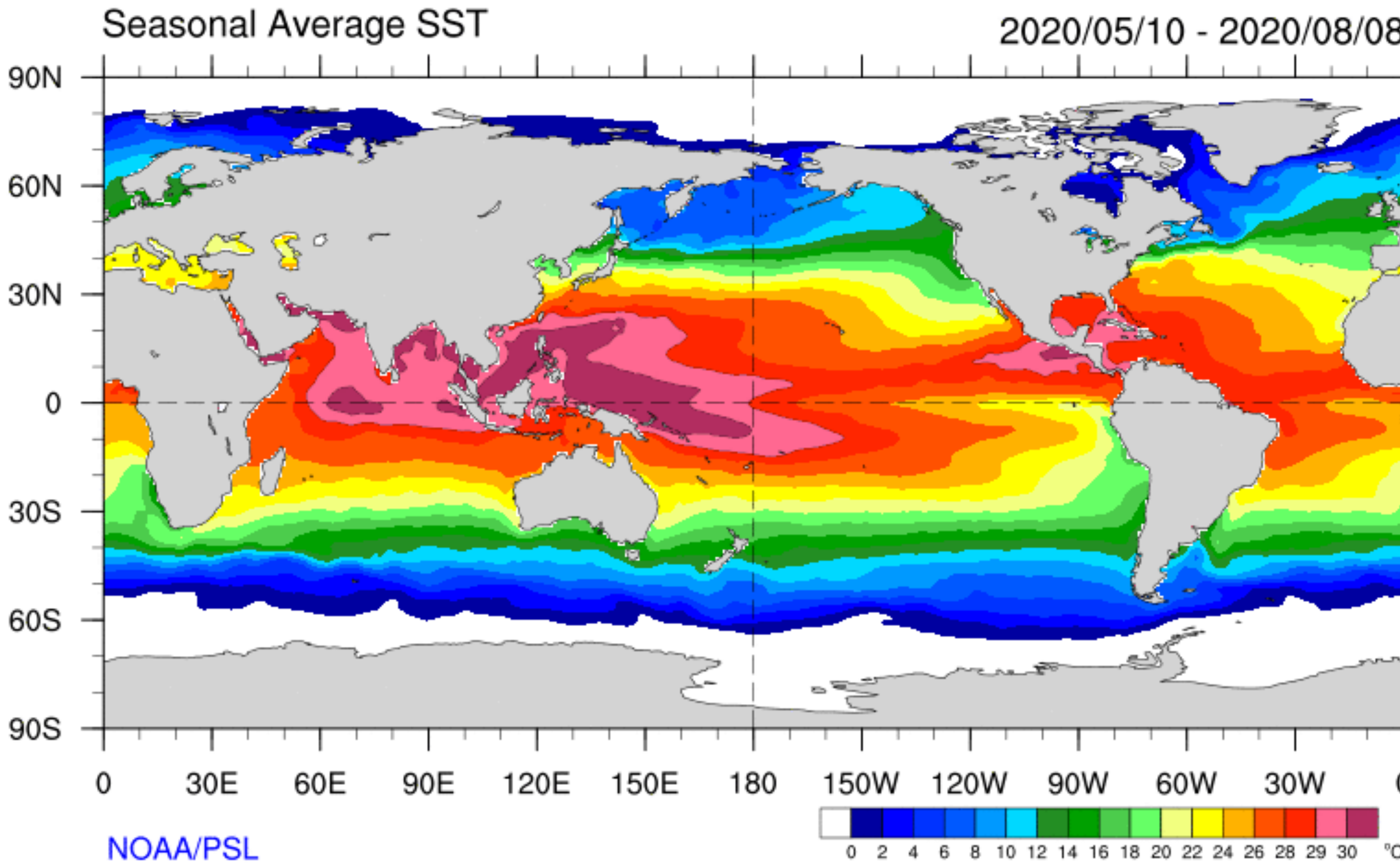

Seasonal Average SST
2020/05/10 - 2020/08/08
90N
60N
30N
0
30S
60S
90S
0
30E
60E
90E
120E
150E
180
150W
120W
90W
60W
30W
0
0 2 4 6 8 10 12 14 16 18 20 22 24 26 28 29 30
°C
NOAA/PSL

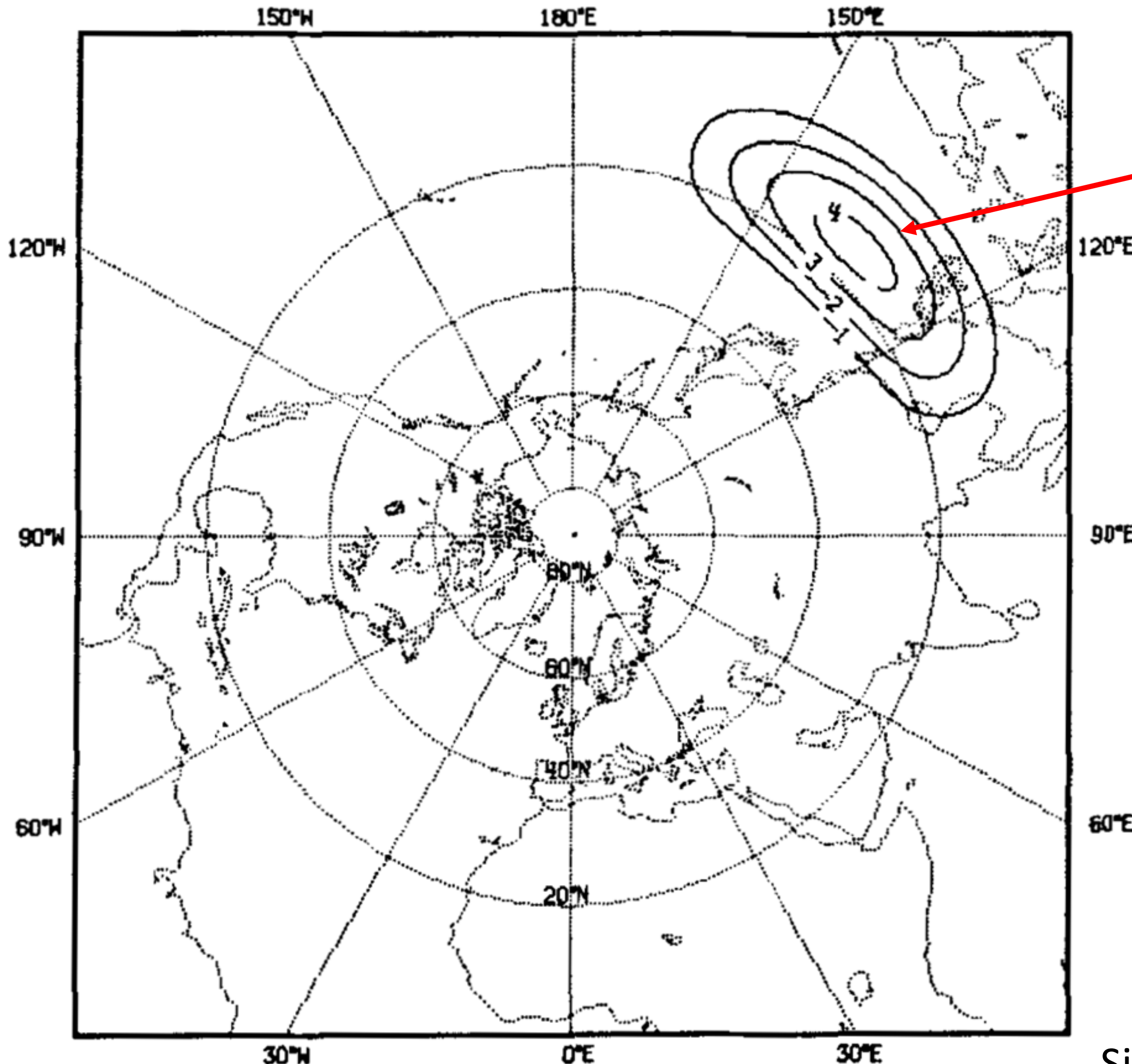

Prescribe a tropical heat anomaly and see what the extratropical response is.

Simmons (1982)

Figure 1. The horizontal distribution of diabatic heating given analytically by Eq. (9) with a maximum value of 5 units.

Response to the heating anomaly:

Barotropic in structure (i.e. it is not dependent on height)

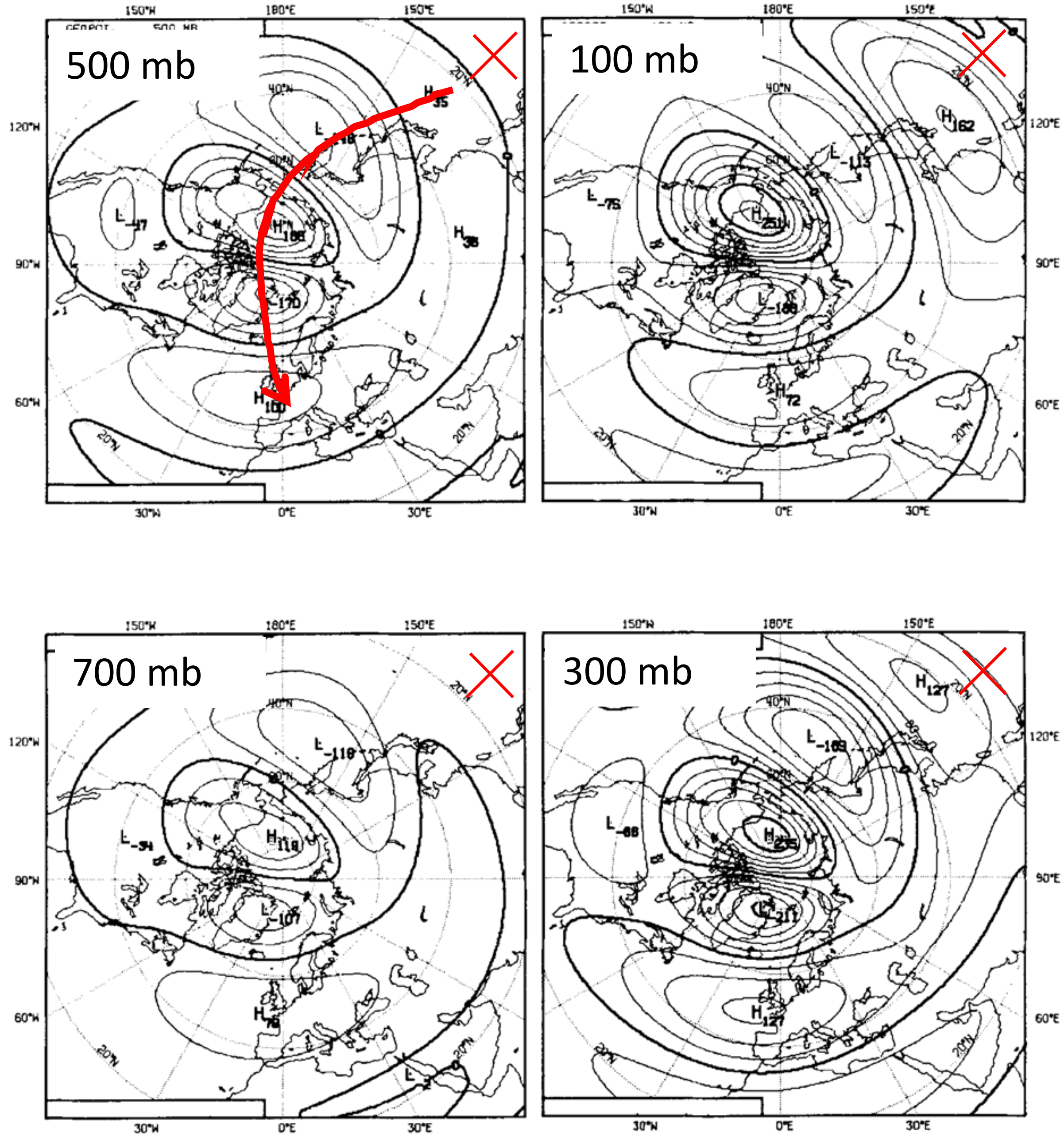

Simmons (1982)

Figure 3. The response to heating centred at 15 °N, 135 °E. The perturbation geopotential is shown at 700 mb (lower left), 500 mb (upper left), 300 mb (lower right) and 100 mb (upper right). The contour interval is 4 dam.

Seasonal dependence of mid-latitude response

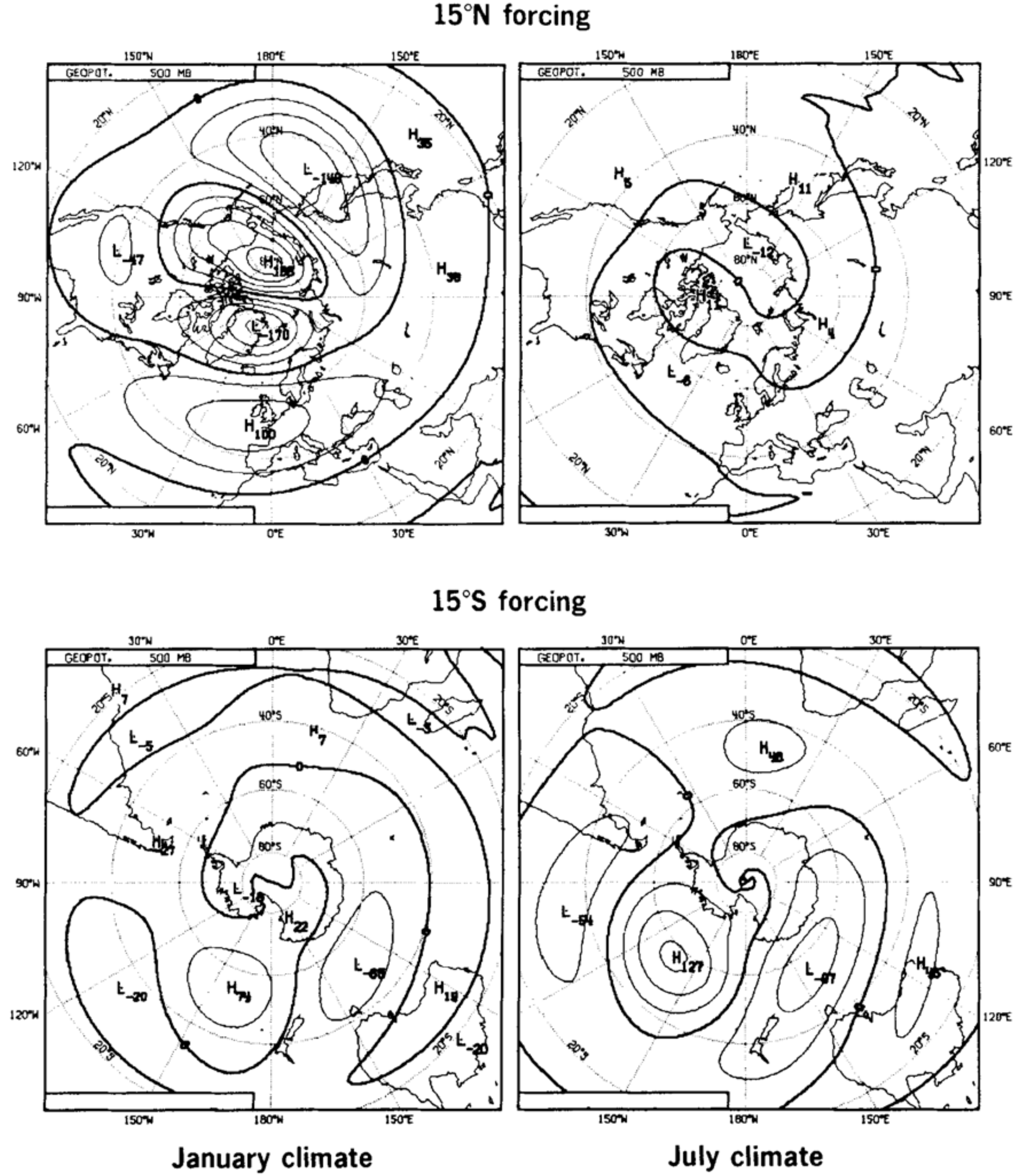

Figure 5. The 500 mb response for the Northern Hemisphere (upper, heating centred at 15 °N) and the Southern Hemisphere (lower, heating centred at 15 °S). Results are presented for January (left) and July (right) climatological mean states.

Simmons (1982)

Dependence on latitude of forcing.

If forcing is near equatorial, mean easterlies act to ”trap” disturbances. Also f is small, so vorticity generation by equatorial disturbances is lower.

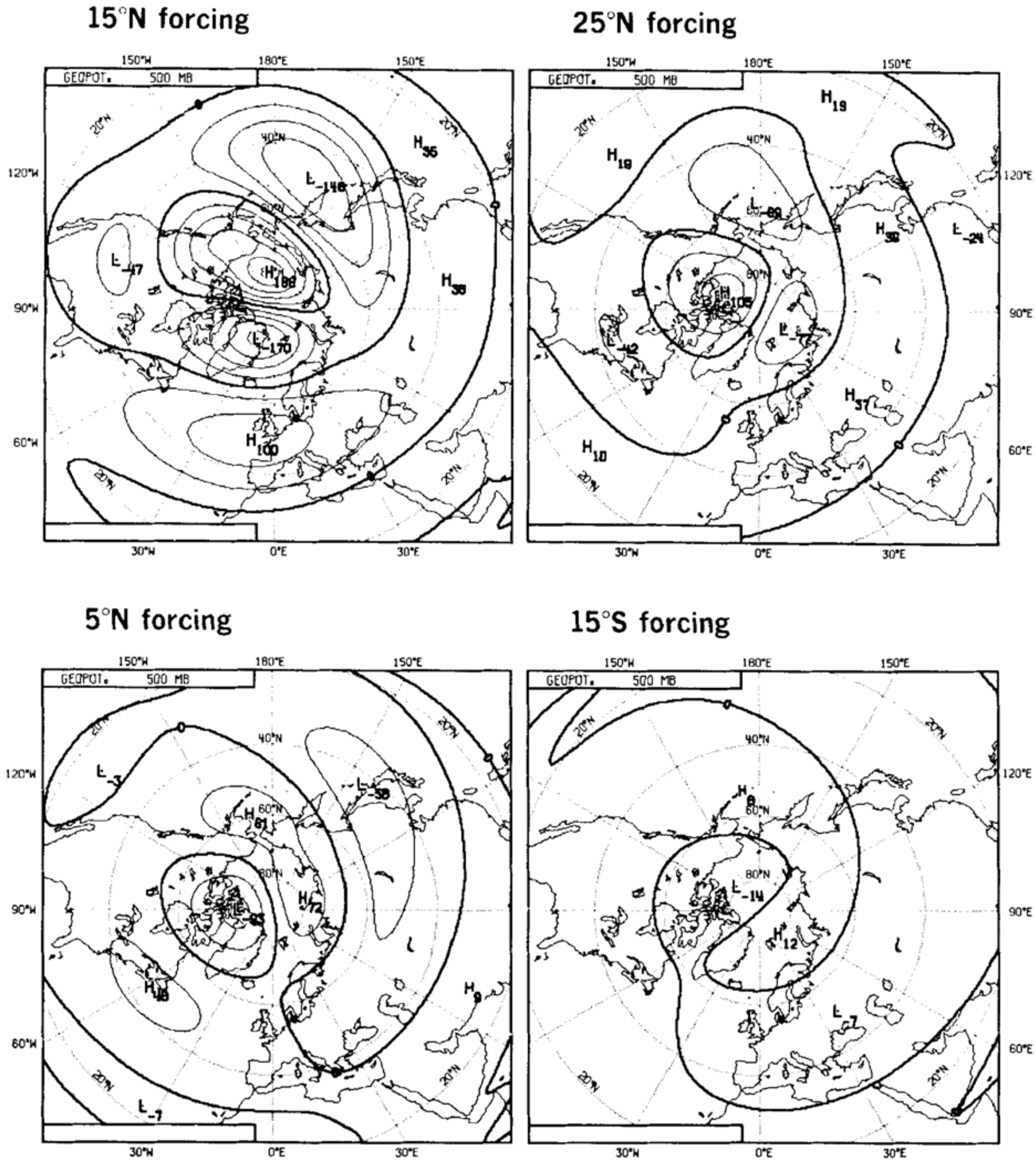

Figure 6. 500 mb height perturbations for heatings centred at 135 °E and various latitudes.

Simmons (1982)

$$\omega = \bar{u}_M k - \frac{\beta_M k}{k^2 + l^2}$$

$$u_g = \frac{\partial \omega}{\partial k} = \frac{\omega}{k} + \frac{2\beta_M k^2}{(k^2 + l^2)^2}$$

$$v_g = \frac{\partial \omega}{\partial l} = \frac{2\beta_M k l}{(k^2 + l^2)^2} .$$

Taking $\omega = 0$ (stationary wave):

$$\bar{u}_M = \frac{u}{\cos \phi}$$

$$K_s = \sqrt{\frac{\beta_M}{\bar{u}_M}} = \sqrt{k^2 + l^2}$$

$$c_g = 2 \frac{k}{K_s} \bar{u}_M .$$

Dispersion relation from Hoskins and Karoly (1981)

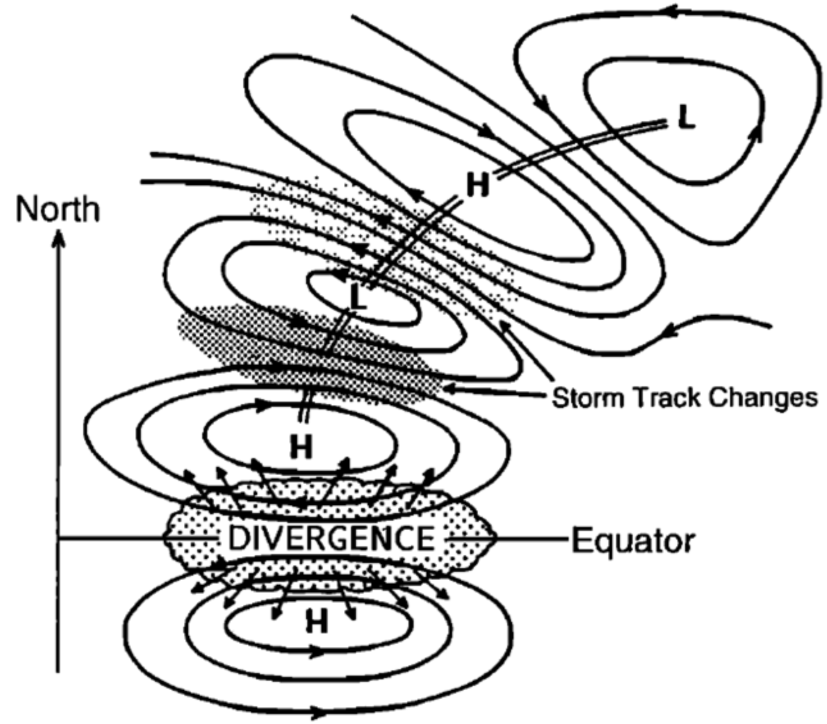

Figure 4. Schematic view of the dominant changes in the upper troposphere, mainly in the northern hemisphere, in response to increases in SSTs, enhanced convection, and anomalous upper tropospheric divergence in the vicinity of the equator (scalloped region). Anomalous outflow into each hemisphere results in subtropical convergence and an anomalous anticyclone pair straddling the equator, as indicated by the streamlines. A wave train of alternating high and low geopotential and streamfunction anomalies results from the quasi-stationary Rossby wave response (linked by the double line). In turn, this typically produces a southward shift in the storm track associated with the subtropical jet stream, leading to enhanced storm track activity to the south (dark stipple) and diminished activity to the north (light stipple) of the first cyclonic center. Corresponding changes may occur in the southern hemisphere.

Figure: Trenberth et al. (1998)

ENSO forcings

WARM EPISODE RELATIONSHIPS

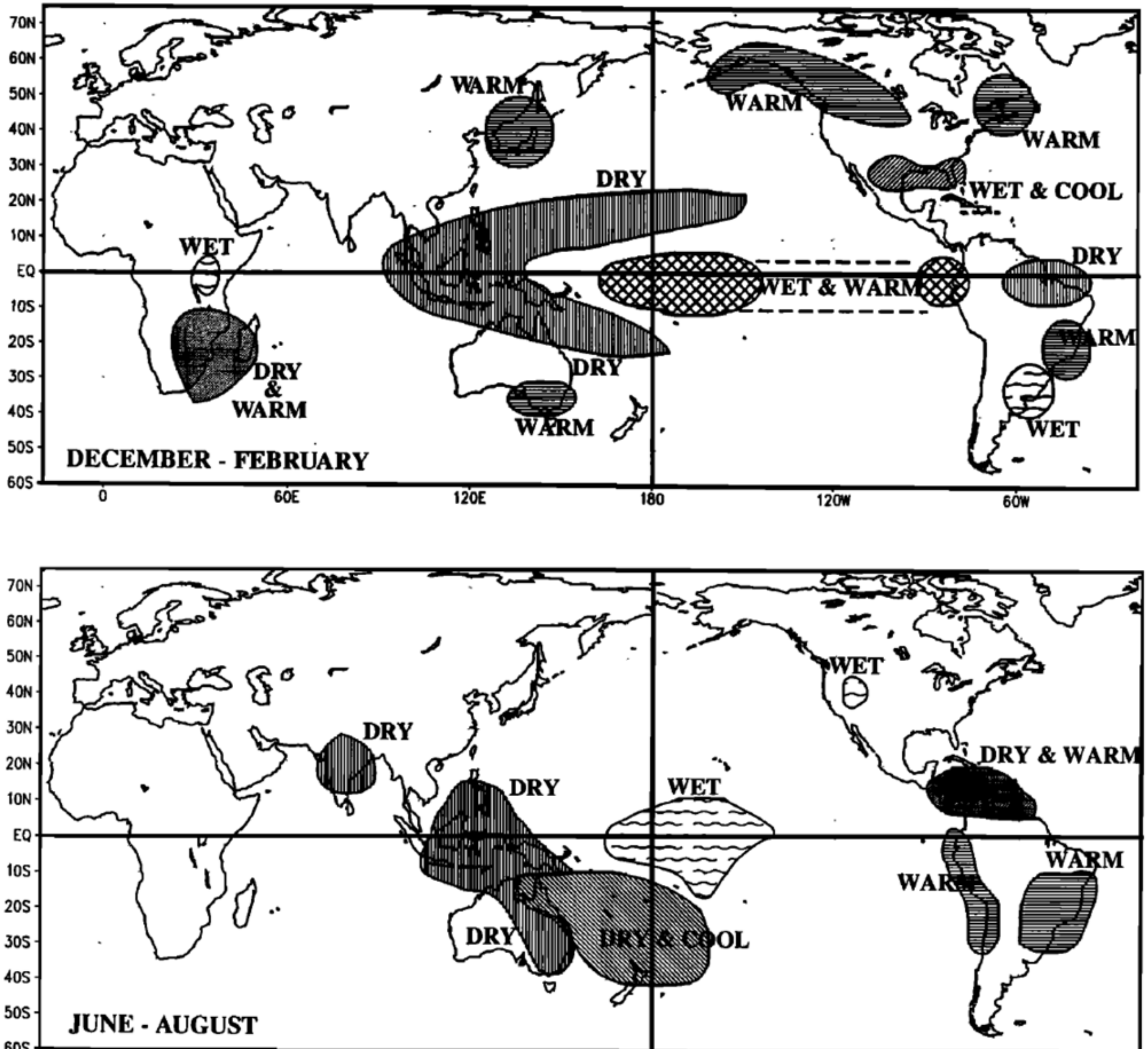

Figure 2. Schematic of temperature and precipitation anomalies generally associated with the warm phase of El Niño-Southern Oscillation (ENSO) during the northern winter and summer seasons. To a good approximation, relationships with the cold phase of ENSO are simply reversed in sign. (After *Ropelewski and Halpert* [1986, 1987, 1989] and *Halpert and Ropelewski* [1992] and supplemented by *Aceituno* [1988].)

Trenberth et al. (1998)

DJF 1986–87
(El Niño)

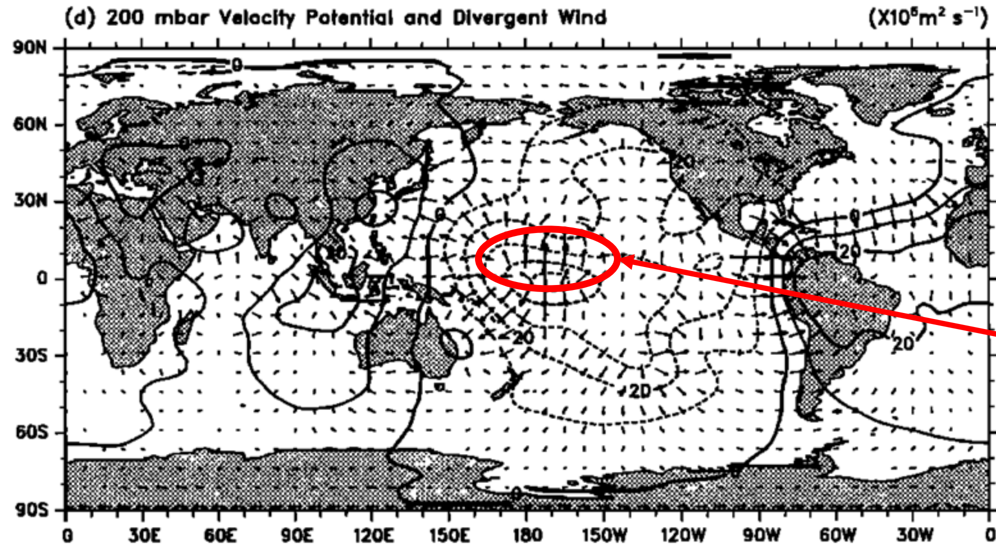

Divergent anomaly aloft associated with enhanced central Pacific convection

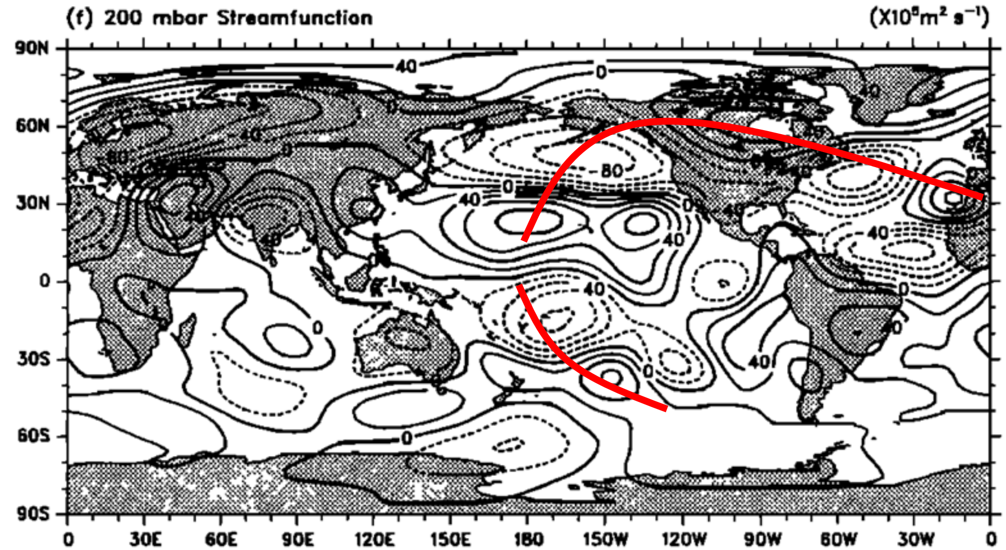

Northern and Southern Hemisphere Rossby wave trains

Trenberth et al. (1998)

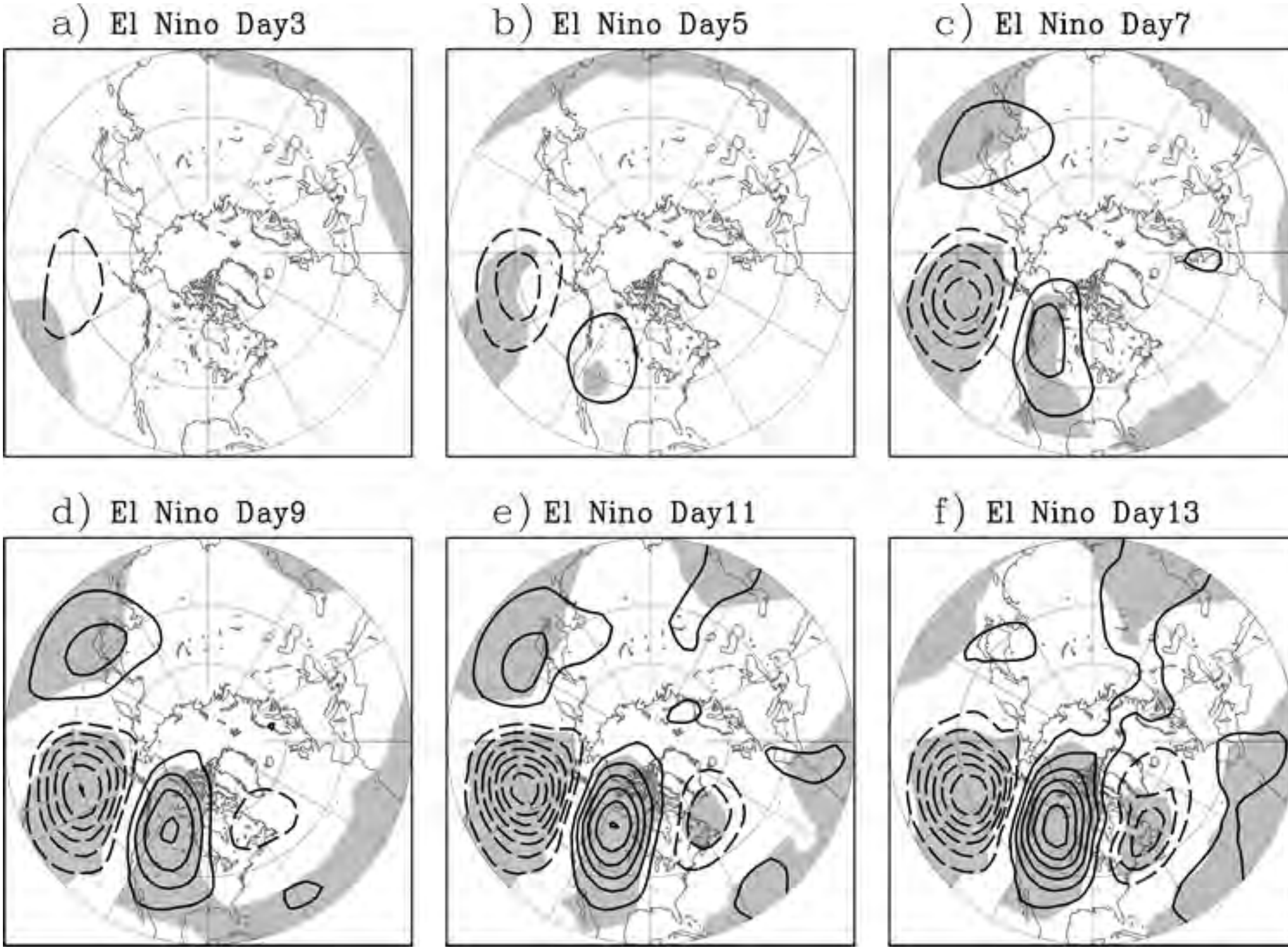

H. Lin et al. (2007); *JCLI*

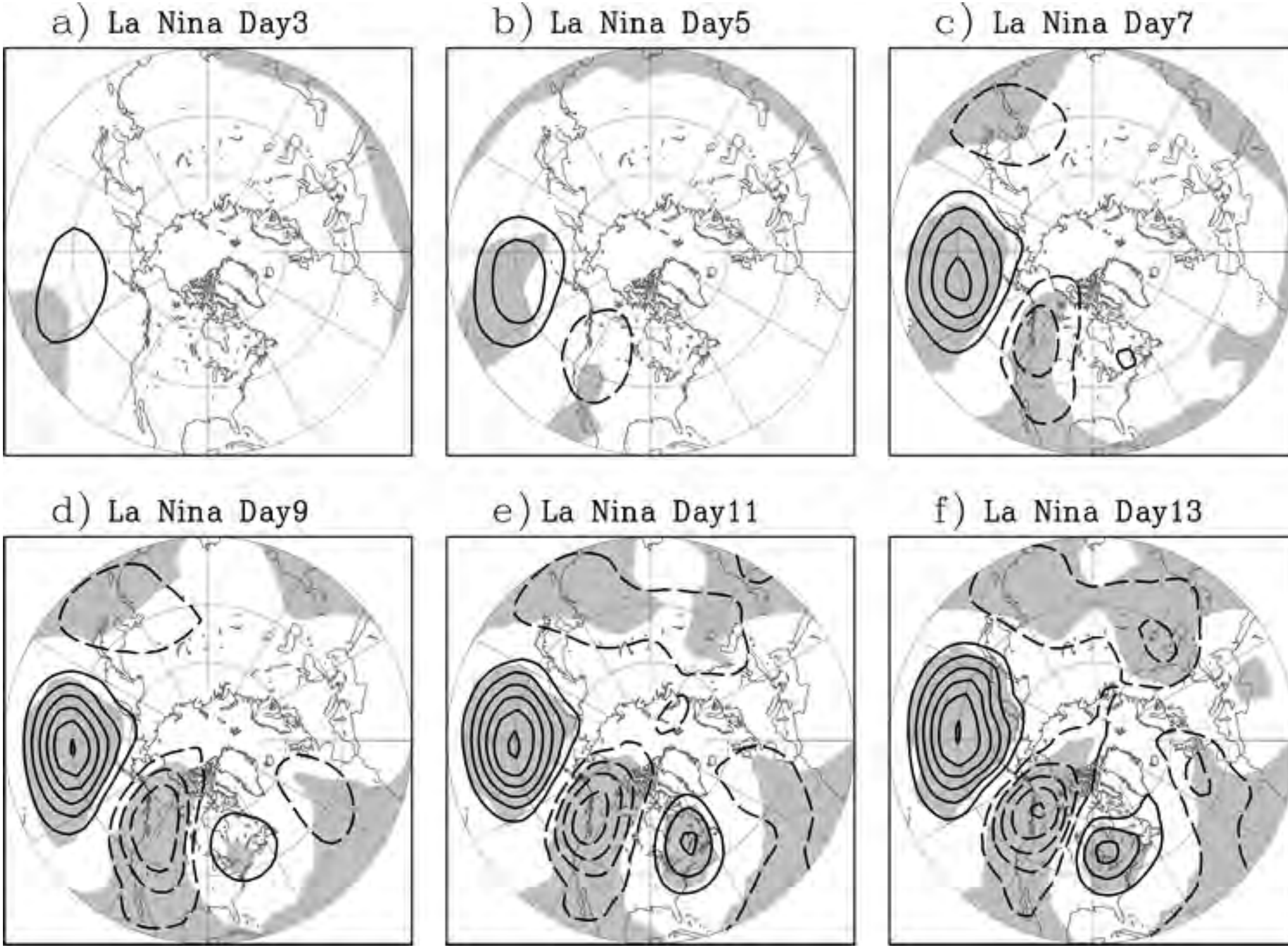

Lin et al. (2007)

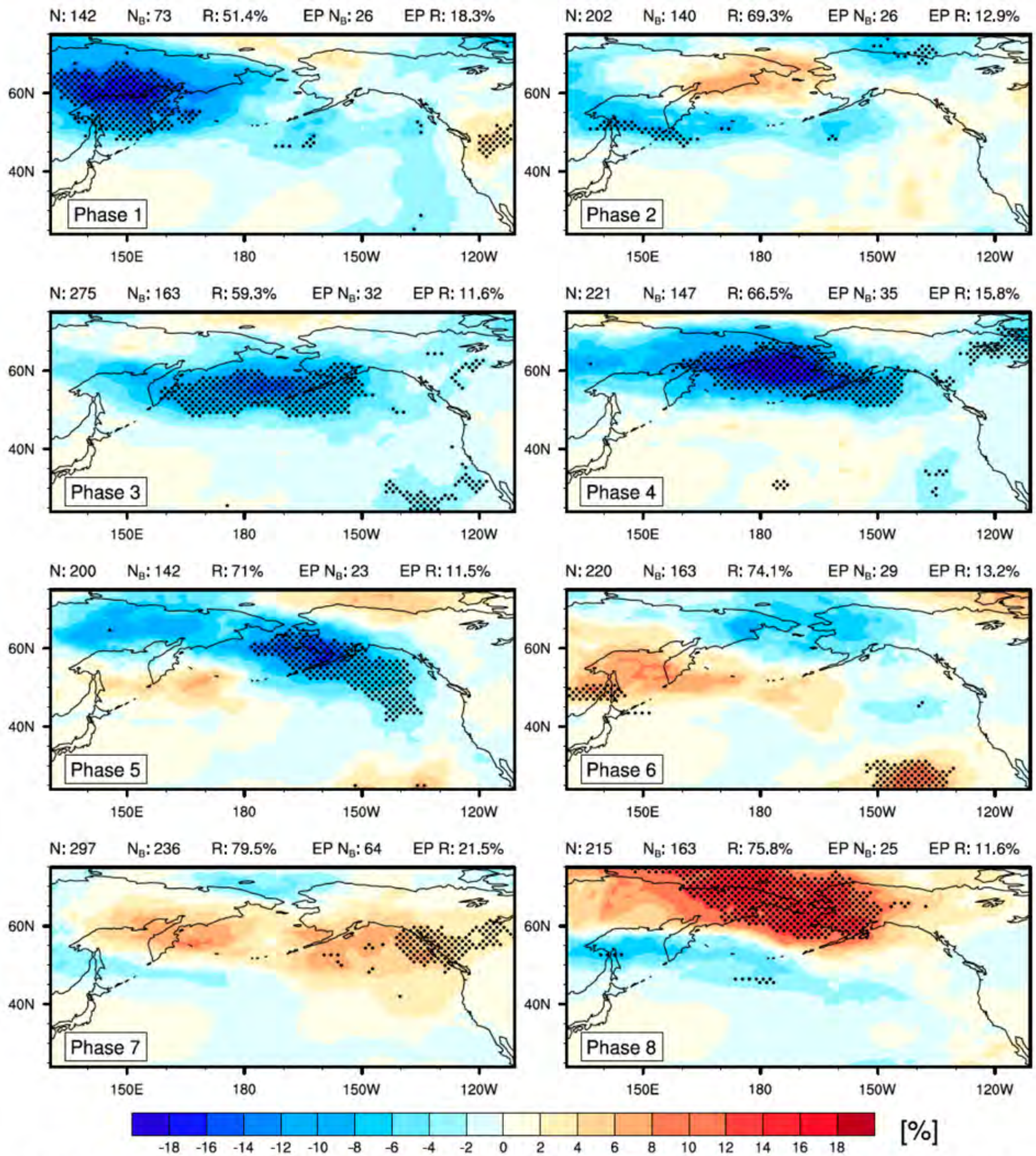

FIG. 2. Pacific blocking frequency anomalies at lag 0 for each phase of the MJO as determined by Eq. (1). Blocking frequencies are shown as a deviation from the DJF mean (Fig. 1). Black dotting demonstrates the anomalies found to be 95% significantly different from zero. For explanation of the values above each panel, see section 2c.

Henderson et al. (2016)

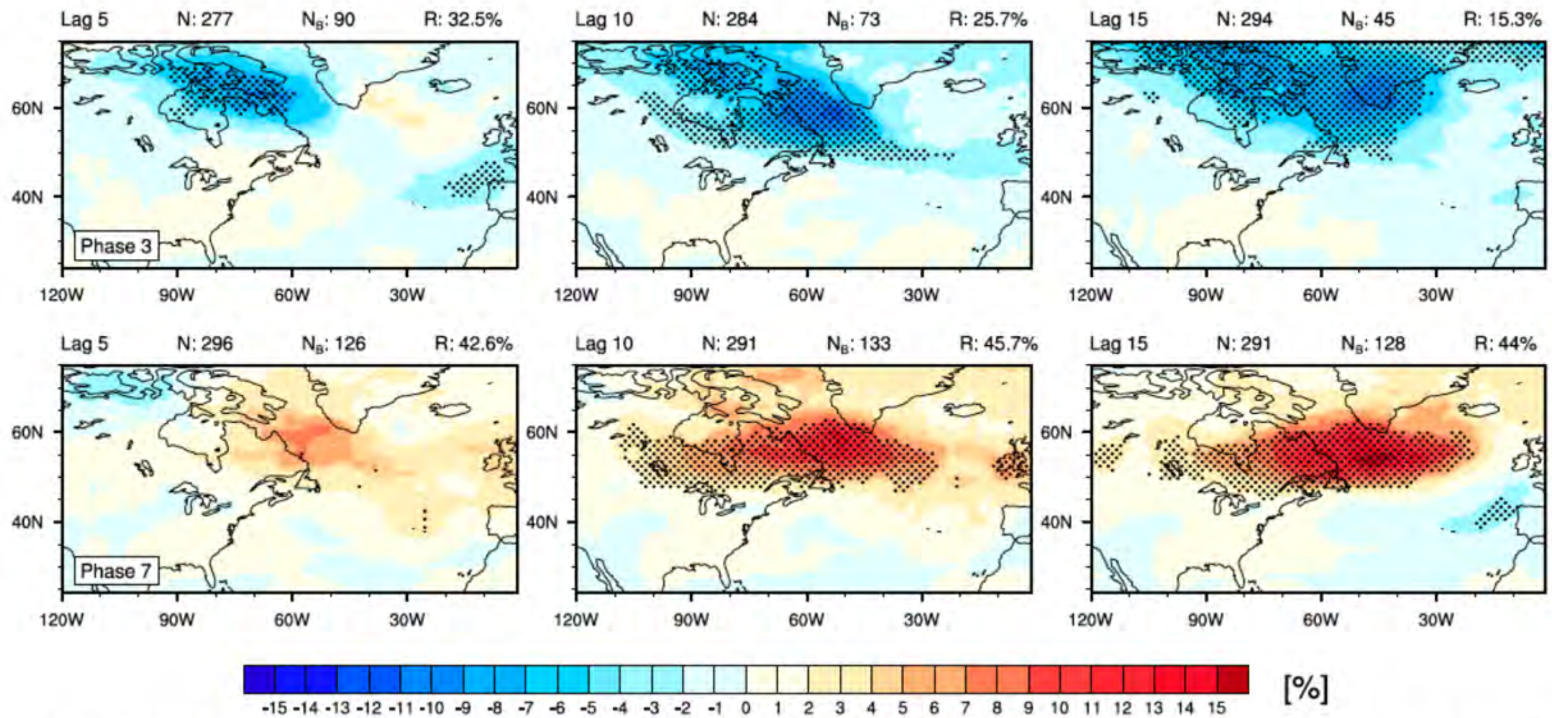

FIG. 7. Atlantic blocking frequency anomalies as determined by Eq. (1) for MJO phases (top) 3 and (bottom) 7. Shown are (left) lag 5, (middle) lag 10, and (right) lag 15, where a lag *n* represents the blocking frequency *n* days after the MJO phase. Blocking frequencies are shown as a deviation from the DJF mean. Black dotting demonstrates the anomalies found to be 95% significantly different from zero. For explanation of the values above each panel, see section 2c.

Henderson et al. (2016)

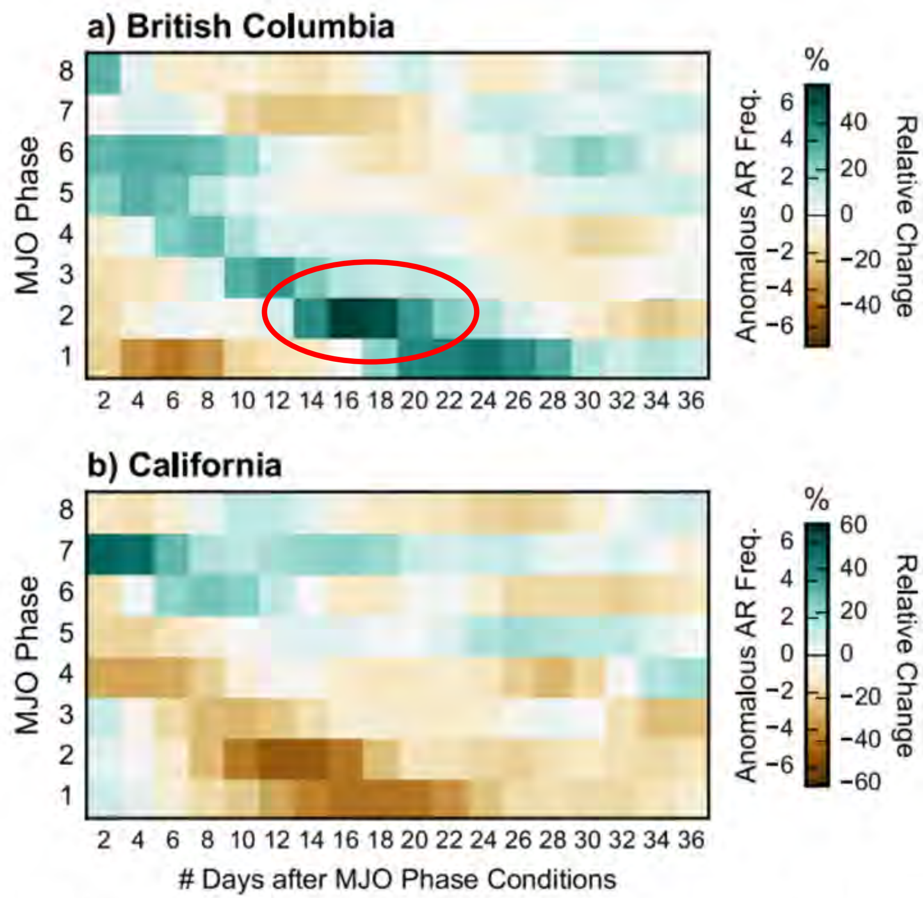

Fig. 2 Composite anomalous AR activity as a function of MJO phase (*y* axis) and number of days after active MJO phase conditions (*x* axis) in terms of anomalous frequency of occurrence (%, left range of colorbar) and the change relative to the location's mean DJFM AR frequency (% change, right range of colorbar) for the (**a**) British Columbia and (**b**) California landfall boundaries

For example, this means that 15–20 days after a strong MJO projects onto RMM Phase 2, AR activity occurs over western Canada.

Mundhenk et al. (2018)

CAPE

0–3 km
Storm
relative
helicity

CAPE * SRH^2

Tornado
events

Hail events

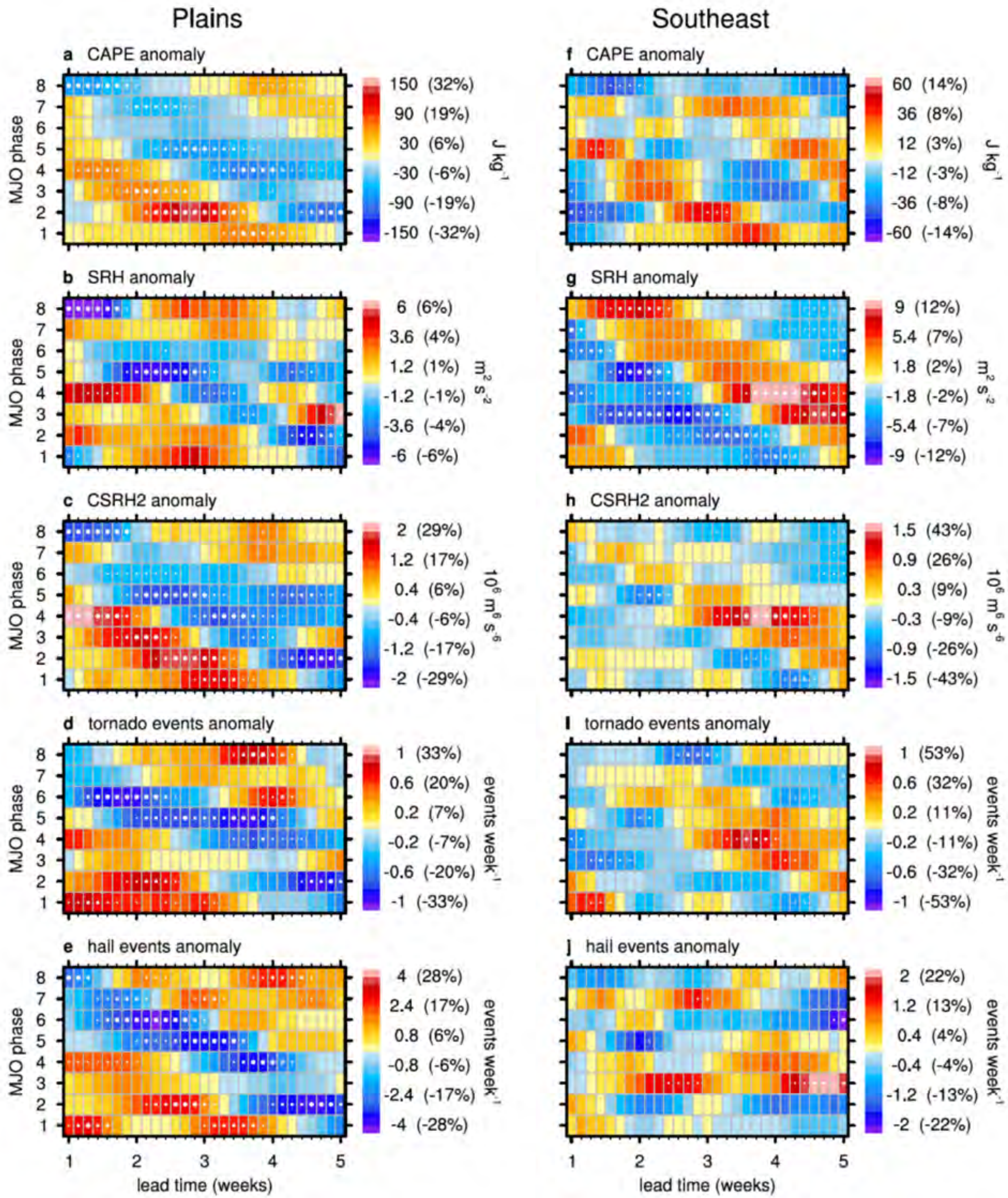

Baggett et al.
(2018)